

Lepton flavor violation in the Majorana and Dirac scotogenic models

Raghavendra Srikanth Hundi

Department of Physics, Indian Institute of Technology Hyderabad,
Kandi - 502 284, India.

E-mail: rshundi@phy.iith.ac.in

Abstract

In this work we have considered two minimal versions of scotogenic models, where neutrinos acquire masses through a radiative mechanism. We call these two models as Majorana and Dirac scotogenic models. In the former model, neutrinos have Majorana nature, and in the later one, neutrinos are Dirac particles. These two models are related to each other in terms of additional fields and symmetries of the model. Hence, to compare these two models in future experiments, we have analyzed lepton flavor violating (LFV) processes in both of them, in the charged lepton sector. We have found that the 3-body LFV decays in both these models can get different contributions. Among all the LFV decays and after satisfying relevant constraints, we have found that $\tau \rightarrow 3\mu$ can have a branching ratio as high as $10^{-10}(10^{-11})$ in the Majorana(Dirac) scotogenic model. This branching ratio can be probed in the future planned experiments.

1 Introduction

From the neutrino oscillation experiments [1, 2] and cosmological data [3], it is known that neutrinos have non-zero and tiny masses. Non-zero masses for neutrinos can be conceived in the standard model by proposing singlet right-handed neutrinos. However, smallness of their masses can be explained only by unnaturally suppressing the Yukawa couplings. As a result of this, to understand the origin of neutrino masses, the standard model should be expanded with new fields and symmetries [4, 5]. Several models have been proposed on the origin of neutrino masses. For instance, see [6, 7] for a review on these models. Most of these models are based on seesaw mechanism [8–15], according to which, conservation of lepton number is violated, and hence, neutrinos are Majorana particles. Whether lepton number is violated or not is not yet known in experiments. As a result of this, models which conserve lepton number are also proposed, according to which neutrinos are Dirac particles. See [16–24] for an early literature of models on Dirac neutrino masses. From the current status of experiments, neutrinos can have either Majorana or Dirac nature and it is still an open problem to know which of these two possibilities is true.

To understand the origin of neutrino masses, a particular class of models, known as scotogenic models are studied. In these models, neutrinos acquire masses through a loop induced mechanism, and as a result of that, loop suppression factor gives a natural suppression for explaining the smallness of neutrino masses. Scotogenic models can be classified into two categories, which depend on if the neutrinos in these models have Majorana or Dirac nature. In the category of scotogenic models, where neutrinos are Majorana particles, there exist extensive literature. In this category, see [25–32], [33–42] and [43, 44] for early models, some recent phenomenological works and our own works, respectively. On the other hand, in the category of scotogenic models, where neutrinos are Dirac particles, see [45–64] for various models and phenomenological works.

Since the scotogenic models are viable in explaining the smallness of neutrino masses, in this work, we consider two minimal versions of these models, which are named as Majorana and Dirac scotogenic models. In the Majorana scotogenic model (MSM) [25], neutrinos are Majorana particles. Whereas in the Dirac scotogenic model (DSM) [45], neutrinos are purely Dirac particles. Both MSM and DSM are extensions to the standard model with new fields and symmetries. In the MSM, the additional fields are the scalar doublet η^M and the singlet Majorana fermions N_k^M , $k = 1, 2, 3$. To achieve loop induced masses to neutrinos in the MSM [25], a discrete symmetry Z_2 is introduced, under which η^M and N_k^M are odd and all the standard model fields are even. On the other hand, in

the DSM [45], the additional fields are the scalar doublet η^D , the singlet scalar χ and the following singlet Weyl fermions: ν_α^c , N_k , N_k^c . Here, $\alpha = e, \mu, \tau$. The fields ν_α^c combine with the left-handed neutrinos of lepton doublets to form Dirac neutrinos and N_k , N_k^c combine together to form Dirac fermions N_k^D in the DSM. To generate radiative masses to Dirac neutrinos in this model [45], a discrete symmetry $Z_2^{(A)} \times Z_2^{(B)}$ is proposed, under which all the above described fields are charged and the standard model fields are even. From the description given above for both the MSM and DSM, we see that there is a similarity between these two models in terms of field content and symmetries. In fact, note that, we have used the suffixes M and D to distinguish similar fields in the MSM and DSM. Since these models are similar to each other, it is worth to compare observable quantities of these two models, which is one of the aims of the current work.

As described above, the MSM and DSM can address the problem of origin of neutrino masses. The other problem that needs to be addressed in these models is related to the neutrino mixing angles, which is described below. From the oscillation data [65], it is known that there exists two large mixing angles and one small mixing angle in the neutrino sector. A consequence of these mixing angles is that the mass matrix for neutrinos in the flavor basis will have nonzero off-diagonal elements. Such a structure of mass matrix can be explained in the MSM and DSM, only if the Yukawa couplings of the lepton doublets have off-diagonal elements. We demonstrate this statement explicitly in the next section. Generally, the off-diagonal elements of Yukawa couplings drive lepton flavor violating (LFV) processes such as $\ell_\alpha \rightarrow \ell_\beta \gamma$, $\ell_\alpha \rightarrow \ell_\beta \ell_\rho \bar{\ell}_\delta$ and $\mu N \rightarrow e N$. Here, N is a nucleus. Although these LFV processes take place in the MSM and DSM, none of these processes are observed in experiments. Moreover, upper bounds are set on the branching ratios of these processes due to non-observation of them in experiments. In Tab. 1 we have tabulated the upper bounds obtained on the above described LFV processes, which have been searched in experiments. The upper bounds given in Tab. 1 give constraints on the model parameters of a model. In the present work, our aim is to study the LFV processes and the constraints due to non-observation of these processes in the MSM and DSM. In addition to this, we compare the contributions of the LFV processes which give rise in these models, and that would be helpful in distinguishing these two models in future experiments. In our study, we have found that the 3-body muon and tau decays, which are mentioned in Tab. 1, can give rise to different contributions in both these models. Hence, there is a possibility to distinguish these two models by searching the above mentioned decays in future experiments. On the other hand, the 2-body muon and tau decays, which are mentioned in Tab. 1, may give similar contributions in both these

LFV process	current bound
$\mu^+ \rightarrow e^+\gamma$	3.1×10^{-13} [66]
$\tau^\pm \rightarrow e^\pm\gamma$	3.3×10^{-8} [67]
$\tau^\pm \rightarrow \mu^\pm\gamma$	4.2×10^{-8} [68]
$\mu^+ \rightarrow e^+e^+e^-$	1.0×10^{-12} [69]
$\tau^- \rightarrow e^-e^-e^+$	2.7×10^{-8} [70]
$\tau^- \rightarrow e^-\mu^-\mu^+$	2.7×10^{-8} [70]
$\tau^- \rightarrow \mu^-\mu^-e^+$	1.7×10^{-8} [70]
$\tau^- \rightarrow e^-\mu^-e^+$	1.8×10^{-8} [70]
$\tau^- \rightarrow e^-e^-\mu^+$	1.5×10^{-8} [70]
$\tau^- \rightarrow \mu^-\mu^-\mu^+$	2.1×10^{-8} [70]
$\mu^- \text{Au} \rightarrow e^- \text{Au}$	7×10^{-13} [71]
$\mu^- \text{Ti} \rightarrow e^- \text{Ti}$	4.3×10^{-12} [72]

Table 1: Experimental upper bounds on various LFV processes. In the second column, the last two entries are upper bounds on the conversion rate of $\mu \rightarrow e$ in the presence of a nucleus. Rest of the entries in this column are upper bounds on the branching ratios of the LFV decays.

models. The details of the above mentioned results will be described later.

LFV processes in the MSM have already been studied previously in [73]. Below we describe the difference of our work in comparison to that of [73]. In [73], among all possible 3-body LFV decays, only the decays of the form $l_\alpha \rightarrow l_\beta l_\beta \bar{l}_\beta$ are analyzed. After comparing with Tab. 1, we notice that other 3-body decays of $l_\tau \rightarrow l_\beta l_\delta \bar{l}_\delta$ and $l_\tau \rightarrow l_\beta l_\beta \bar{l}_\delta$, where $\beta \neq \delta$ and $\beta, \delta = e, \mu$, are also possible in the MSM. However, these decays are not studied in [73]. Hence, in order to complete the analysis on LFV, we have computed branching ratios of the 3-body decays $l_\tau \rightarrow l_\beta l_\delta \bar{l}_\delta$ and $l_\tau \rightarrow l_\beta l_\beta \bar{l}_\delta$ in the MSM and also in the DSM. As already mentioned before, analyzing these 3-body decays is worth to do, since these decays give different contributions in the MSM and DSM, and hence, these models can be distinguished by searching the LFV decays in experiments. In addition to the above described differences, the numerical analysis of work is different from that of [73], which we explain later. In this work, we have analyzed all different LFV processes in the DSM for the first time. In this context, notice that in [56], where the proposed model is closely related to the DSM, the LFV processes driven by the muon are studied but the 3-body tau decays are not studied.

The paper is organized as follows. In the next section, we describe the relevant details of the models which are under consideration of this work. In Sec. 3, we describe different Feynman diagrams that give rise to LFV processes in the MSM and DSM. In Sec. 4, we describe our methodology of computing the amplitudes of the LFV processes and present the analytical expressions of all the LFV processes in the MSM. In Sec. 5, we explain how to translate the analytical expressions of Sec. 4 into corresponding expressions for the case of DSM. In Sec. 6, we present the numerical results obtained in both the MSM and DSM. We conclude in the last section.

2 The models

We have given a brief introduction to the MSM and DSM in the previous section. Here, we describe relevant parts of these models, whose content is useful to us in computing the LFV processes of these models.

2.1 MSM

Relevant fields and symmetries of the MSM [25] are tabulated in Tab. 2. Now, with these

Field	Spin	$SU(2)_L$	$U(1)_Y$	Z_2
$L_\alpha = (\nu_\alpha, \ell_\alpha)$	1/2	2	-1/2	+
ℓ_α^c	1/2	1	1	+
$\Phi^T = (\phi^+, \phi^0)$	0	2	1/2	+
$\eta_M^T = (\eta_M^+, \eta_M^0)$	0	2	1/2	-
N_k^m	1/2	1	0	-

Table 2: Fields in the lepton sector of the MSM along with their charge assignments. Here, Φ is the Higgs-like doublet.

fields and symmetries, the invariant Lagrangian of the model is

$$-\mathcal{L}^M = y_{\alpha\beta}(\nu_\alpha\phi^{+*} + \ell_\alpha\phi^{0*})\ell_\beta^c + f_{\alpha k}^M(\nu_\alpha\eta_M^0 - \ell_\alpha\eta_M^+)N_k^m + \frac{1}{2}M_k N_k^m N_k^m + h.c. \quad (1)$$

Here, M_k is the mass of the Majorana field N_k^M , which is formed from the Weyl fermion N_k^m . After the electroweak symmetry breaking, Φ acquires vacuum expectation value (VEV), and hence, the first term in Eq. (1) gives masses to charged leptons. On the other hand, η_M acquires zero VEV since it is odd under the Z_2 symmetry, and hence, neutrinos

are massless at tree level. Neutrinos acquire masses through a radiative mechanism which is shortly explained later.

The invariant scalar potential between Φ and η_M is given by [25]

$$V_M = m_1^2 \phi^\dagger \phi + m_2^2 \eta^\dagger \eta + \frac{1}{2} \lambda_1 (\phi^\dagger \phi)^2 + \frac{1}{2} \lambda_2 (\eta_M^\dagger \eta_M)^2 + \lambda_3 (\phi^\dagger \phi) (\eta_M^\dagger \eta_M) + \lambda_4 (\phi^\dagger \eta_M) (\eta_M^\dagger \phi) + \frac{1}{2} \lambda_5 [(\phi^\dagger \eta_M)^2 + h.c.]. \quad (2)$$

After minimizing this scalar potential, only the Φ should acquire VEV. Hence, we parameterize the neutral components of Φ and η_M as

$$\phi^0 = \frac{H}{\sqrt{2}} + v, \quad \eta_M^0 = \frac{1}{\sqrt{2}} (\eta_{MR} + i\eta_{MI}) \quad (3)$$

Here, H is the Higgs boson and $v = 174$ GeV. Now, after the electroweak symmetry breaking, the mass spectrum in the MSM is given by [25]

$$\begin{aligned} m^2(H) &\equiv m_H^2 = 2\lambda_1 v^2, \\ m^2(\eta_M^\pm) &\equiv m_{\eta_M^\pm}^2 = m_2^2 + \lambda_3 v^2, \\ m^2(\eta_{MR}) &\equiv m_R^2 = m_2^2 + (\lambda_3 + \lambda_4 + \lambda_5) v^2, \\ m^2(\eta_{MI}) &\equiv m_I^2 = m_2^2 + (\lambda_3 + \lambda_4 - \lambda_5) v^2 \end{aligned} \quad (4)$$

As stated before, neutrinos in the MSM acquire masses through a radiative mechanism. At 1-loop level, the neutral components of η_M and N_k^M drive masses to neutrinos in this model. By taking $\Lambda^M = \text{diag}(\Lambda_1^M, \Lambda_2^M, \Lambda_3^M)$, the mass expressions for neutrinos at 1-loop level can be written as [25]

$$\begin{aligned} (\mathcal{M}_\nu)_{\alpha\beta} &= (f^M \Lambda^M f^{MT})_{\alpha\beta} = \sum_{k=1}^3 f_{\alpha k}^M f_{\beta k}^M \Lambda_k^M, \\ \Lambda_k^M &= \frac{M_k}{16\pi^2} \left[\frac{m_R^2}{m_R^2 - M_k^2} \ln \frac{m_R^2}{M_k^2} - \frac{m_I^2}{m_I^2 - M_k^2} \ln \frac{m_I^2}{M_k^2} \right] \end{aligned} \quad (5)$$

By diagonalizing the above mass matrix, we get the neutrino masses and also the mixing angles. We diagonalize this matrix by parametrizing [74] the Yukawa couplings as

$$f^M = U_{PMNS}^* \sqrt{m_\nu} R \sqrt{\Lambda^M}^{-1} \quad (6)$$

Here, U_{PMNS} is the Pontecorvo-Maki-Nakagawa-Sakata matrix, which can be parameterized [75] in terms of the three neutrino mixing angles, one CP violating Dirac phase and two Majorana phases. m_ν is a diagonal matrix containing the neutrino mass eigenvalues,

which is written as $m_\nu = \text{diag}(m_1, m_2, m_3)$. R is a complex orthogonal matrix which satisfies $RR^T = I = R^T R$. Now, using the parametrization of Eq. (6), notice that

$$\mathcal{M}_\nu = U_{PMNS}^* m_\nu U_{PMNS}^\dagger \quad (7)$$

From the above equation, we see that the unitary matrix that diagonalize \mathcal{M}_ν is U_{PMNS} . Hence, the mixing angles in the neutrino sector of the MSM can be explained by parametrizing the Yukawa couplings as given by Eq. (6).

As stated in Sec. 1, the off-diagonal elements of Yukawa couplings drive LFV processes. Without loss of generality, the Yukawa couplings $y_{\alpha\beta}$ of Eq. (1) can be taken to be diagonal. On the other hand, the Yukawa couplings f^M , whose form is given in Eq. (6), have off-diagonal elements, since U_{PMNS} is off-diagonal. As these couplings determine the strength of the LFV processes, below we give an estimation of when these couplings become large enough. In the expression for f^M , R has no physical interpretation. Hence, to simplify our analysis, we take $R = I$. As a result of this, the expression for f^M becomes

$$f^M = U_{PMNS}^* \cdot \text{Diag} \left(\sqrt{\frac{m_1}{\Lambda_1^M}}, \sqrt{\frac{m_2}{\Lambda_2^M}}, \sqrt{\frac{m_3}{\Lambda_3^M}} \right) \quad (8)$$

Now we see that, the elements of U_{PMNS} have magnitude of $\mathcal{O}(1)$. On the other hand, the neutrino masses are tiny and hence the couplings $f_{\alpha k}^M$ can become very small. To compensate the small values in $f_{\alpha k}^M$ we can make Λ_k^M to be very small. Notice that this is possible by taking degenerate values for m_R and m_I in Eq. (5), which in turn is possible by suppressing the coupling λ_5 , and this can be noticed from Eq. (4). Finally, we have estimated that λ_5 should be suppressed to around 10^{-10} in order to make $f_{\alpha k}^M \sim 1$. While making this estimation, we have taken neutrino mass scale to be around 0.1 eV [75] and the masses of additional fields to be ~ 1 TeV. Hence, for the above described values of parameters, LFV processes in the MSM are unsuppressed and can have significant effects in experiments.

2.2 DSM

Relevant fields and symmetries of the DSM [45] are tabulated in Tab. 3. Here, the symmetry $U(1)_{B-L}$ is exact [45], and without loss of generality we have taken this to be global. The purpose of this symmetry is to have the lepton number be conserved in the DSM. Hence, neutrinos in this model are Dirac particles. The field Φ in Tab. 3 is the Higgs-like doublet, whereas, η_D and χ are the additional scalar fields of this model. Notice that η_D in this model is the analog of η_M of the MSM. Moreover, after comparing

Field	Spin	$SU(2)_L$	$U(1)_Y$	$U(1)_{B-L}$	$Z_2^{(A)}$	$Z_2^{(B)}$
$L_\alpha = (\nu_\alpha, \ell_\alpha)$	1/2	2	-1/2	-1	+	+
ℓ_α^c	1/2	1	1	1	+	+
ν_α^c	1/2	1	0	1	-	+
$\Phi^T = (\phi^+, \phi^0)$	0	2	1/2	0	+	+
$\eta_D^T = (\eta_D^+, \eta_D^0)$	0	2	1/2	0	+	-
χ	0	1	0	0	-	-
N_k	1/2	1	0	-1	+	-
N_k^c	1/2	1	0	1	+	-

Table 3: Fields in the lepton sector of the DSM, along with their charge assignments.

the fields between Tabs. 2 and 3, we see that two different Weyl fermions N_k and N_K^c are introduced in the DSM as against to N_k^m in the MSM. Also notice that the discrete symmetry Z_2 of the MSM has been modified to $Z_2^{(A)} \times Z_2^{(B)}$ in the DSM. Now, with the charge assignments of Tab. 3, the allowed interaction terms in the DSM are

$$-\mathcal{L}^D = y_{\alpha\beta}(\nu_\alpha\phi^{+\ast} + \ell_\alpha\phi^{0\ast})\ell_\beta^c + f_{k\alpha}^D(\nu_\alpha\eta_D^0 - \ell_\alpha\eta_D^+)\mathcal{N}_k^c + h_{\alpha k}N_k\nu_\alpha^c\chi + M'_kN_kN_k^c + h.c. \quad (9)$$

Here, M'_k is the Dirac mass for $N_k^D = (N_k, N_k^c)$. Since Φ acquires VEV, the first term of Eq. (9) give masses to charged leptons in the DSM. On the other hand, η_D and χ do not acquire VEVs, since they are charged under the $Z_2^{(B)}$, which is an exact symmetry. As a result of this, the second and third terms of Eq. (9) do not generate masses to neutrinos at tree level. Shortly later, we explain that, due to soft breaking of the $Z_2^{(A)}$ symmetry, neutrinos acquire masses at 1-loop level in the DSM.

The scalar potential in the DSM is [45]

$$\begin{aligned} V = & \mu_1^2\Phi^\dagger\Phi + \mu_2^2\eta_D^\dagger\eta_D + \frac{1}{2}\mu_3^2\chi^2 + \frac{1}{2}\lambda'_1(\Phi^\dagger\Phi)^2 + \frac{1}{2}\lambda'_2(\eta_D^\dagger\eta_D)^2 + \lambda'_3(\Phi^\dagger\Phi)(\eta_D^\dagger\eta_D) \\ & + \lambda'_4(\Phi^\dagger\eta_D)(\eta_D^\dagger\Phi) + \frac{1}{2}[\lambda'_5(\Phi^\dagger\eta_D)^2 + h.c.] + \frac{1}{4}\lambda'_6\chi^4 + \frac{1}{2}\lambda'_7(\Phi^\dagger\Phi)\chi^2 + \frac{1}{2}\lambda'_8(\eta_D^\dagger\eta_D)\chi^2 \\ & + A\chi[\Phi^\dagger\eta_D + h.c.] \end{aligned} \quad (10)$$

Notice that we have used prime on the parameters in the above potential in order to distinguish these with the corresponding parameters of Eq. (2). In the last term of this potential, without loss of generality, the parameter A is chosen to be real. Moreover, the parameter λ'_5 is also taken to be real in order to simplify our calculations. After minimizing the above scalar potential, only the Φ should acquire VEV, which give rise to

the breaking of the electroweak symmetry. After this symmetry breaking, we identify the real part of the neutral component of Φ as the Higgs boson. Moreover, neutral components of η_D mix with χ . Hence, we write $\eta_D^0 = (\eta_{DR}^0 + i\eta_{DI}^0)/\sqrt{2}$. Now, the mass spectrum of the physical scalar fields in the DSM is [45]

$$\begin{aligned}
m^2(H) &\equiv m_H^2 = 2\lambda'_1 v^2, \\
m^2(\eta_D^\pm) &\equiv m_{\eta_D^\pm}^2 = \mu_2'^2 + \lambda'_3 v^2, \\
m^2(\eta_{DI}^0) &\equiv m_{\eta_{DI}^0}^2 = \mu_2'^2 + (\lambda'_3 + \lambda'_4 - \lambda'_5) v^2, \\
M_{\eta_{DR}^0, \chi}^2 &= \begin{pmatrix} m_{\eta_{DR}^0}^2 & \sqrt{2}Av \\ \sqrt{2}Av & m_\chi^2 \end{pmatrix} \\
m_{\eta_{DR}^0}^2 &= \mu_2'^2 + (\lambda'_3 + \lambda'_4 + \lambda'_5) v^2, \quad m_\chi^2 = \mu_3'^2 + \lambda'_7 v^2
\end{aligned} \tag{11}$$

Here, $M_{\eta_{DR}^0, \chi}^2$ gives the mixing masses between η_{DR}^0 and χ . After diagonalizing this, we denote the mass eigenstates as $\zeta_{1,2}$. Moreover, the mixing between η_{DR}^0 and χ is given by

$$\tan 2\theta = \frac{2\sqrt{2}Av}{m_\chi^2 - m_{\eta_{DR}^0}^2} \tag{12}$$

As described before, in the DSM, neutrinos acquire masses at 1-loop level. The 1-loop diagrams for neutrinos are driven by N_k^D , χ and neutral components of η_D . In order for these loops to exist, soft breaking of the $Z_2^{(A)}$ symmetry is necessary, which happens due to the A -term of Eq. (10). Now, after evaluating these 1-loop diagrams, mass expressions for neutrinos are given by [45]

$$\begin{aligned}
(\mathcal{M}_\nu)_{\alpha\beta} &= (h\Lambda^D f^D)_{\alpha\beta} = \sum_{k=1}^3 h_{\alpha k} \Lambda_k^D f_{k\beta}^D, \\
\Lambda_k^D &= \frac{\sin(2\theta)}{32\pi^2\sqrt{2}} M_k' \left[\frac{m_{\zeta_1}^2}{m_{\zeta_1}^2 - M_k'^2} \ln \frac{m_{\zeta_1}^2}{M_k'^2} - \frac{m_{\zeta_2}^2}{m_{\zeta_2}^2 - M_k'^2} \ln \frac{m_{\zeta_2}^2}{M_k'^2} \right]
\end{aligned} \tag{13}$$

Here, m_{ζ_1} and m_{ζ_2} are the masses of ζ_1 and ζ_2 , whose discussion is given previously. By diagonalizing the above mass matrix, we get neutrino mass eigenvalues and also mixing angles. We diagonalize this matrix by parametrizing [74] the Yukawa couplings as

$$\begin{aligned}
f^D &= \sqrt{\Lambda^{D-1}} S \sqrt{m_\nu} U_{PMNS}^\dagger, \quad h = V \sqrt{m_\nu} R^\dagger \sqrt{\Lambda^D}^{-1}, \\
m_\nu &= \text{diag}(m_1, m_2, m_3)
\end{aligned} \tag{14}$$

Here, R and S are complex matrices which satisfy $R^\dagger S = I$. In fact, after using Eq. (14) in Eq. (13) we get $V^\dagger \mathcal{M}_\nu U_{PMNS} = m_\nu$, which is the desired relation for diagonalizing the

neutrino mass matrix in the DSM. Here, V is a unitary matrix which rotate the right-handed neutrino fields from flavor to mass eigenstates. As described before, the U_{PMNS} matrix is parameterized in terms of neutrino mixing angles and CP violating phases. Hence, by parametrizing the Yukawa couplings as in Eq. (14), we not only obtain the neutrino mass eigenvalues but also the mixing angles. The above described results are analogs of the corresponding results described in Sec. 2.1.

Notice that, from Eq. (14), the Yukawa couplings f^D and h can in general have off-diagonal elements, and hence, they can drive LFV processes. However, the couplings $h_{\alpha k}$ do not drive LFV processes of our interest, at least at 1-loop level, since these couplings connect singlet fields. On the other hand, the couplings $f_{k\alpha}^D$ drive LFV processes of Tab. 1 at 1-loop level. In the expressions of f^D and h , R and S have no physical interpretations. Hence, to simplify our analysis, we take $R = S = I$. As a result of this, the expression for f^D becomes

$$f^D = \text{Diag} \left(\sqrt{\frac{m_1}{\Lambda_1^D}}, \sqrt{\frac{m_2}{\Lambda_2^D}}, \sqrt{\frac{m_3}{\Lambda_3^D}} \right) \cdot U_{PMNS}^\dagger \quad (15)$$

Now, in order not to suppress LFV processes in the DSM, we should have $f_{k\alpha}^D \sim 1$. This possibility can be achieved if $\Lambda_k^D \sim m_i$, since the elements of U_{PMNS} are of order one. As the neutrino masses m_i are tiny, Λ_k^D should be very small in order to achieve the above possibility. From the form of Λ_k^D , which is given in Eq. (13), we see that the above possibility becomes true if either θ or $m_{\zeta_1} - m_{\zeta_2}$ is suppressed, for $m_{\zeta_1}, m_{\zeta_2}, M'_k \sim 1$ TeV. In order to suppress $m_{\zeta_1} - m_{\zeta_2}$, and thus to bring degenerate masses to $\zeta_{1,2}$, we need to fine tune the parameters of $M_{\eta_{DR}^0, \chi}^2$, which is given in Eq. (11). Instead of fine tuning several parameters of $M_{\eta_{DR}^0, \chi}^2$, we have found it is economical to suppress θ in order to achieve the above possibility. Since θ is the mixing angle between η_{DR}^0 and χ , notice that this angle is proportional to the A -parameter. As described previously, the A -parameter breaks the $Z_2^{(A)}$ symmetry softly. Hence, it is technically natural to take this parameter to be small. Finally, in order to achieve $f_{k\alpha}^D \sim 1$, $m_i \sim 0.1$ eV and all additional fields to have around 1 TeV masses, we have found $\theta \sim \frac{A}{v} \sim 10^{-10}$. For these values of parameters, LFV processes in the DSM can have significant effects in experiments.

3 LFV processes in the MSM and DSM

In this section, we describe the Feynman diagrams and various contributions to the LFV processes in both the MSM and DSM. As discussed in Sec. 1, the LFV processes in the charged lepton sector of these two models are categorized into: $l_\alpha \rightarrow l_\beta \gamma$, $l_\alpha \rightarrow l_\beta l_\rho \bar{l}_\delta$

and $\mu N \rightarrow eN$. All these processes take place at 1-loop level in both the MSM and DSM. Moreover, they are driven by common sub-processes, whose Feynman diagrams are given in Fig. 1. The wavy line in this figure represents an off-shell particle, which corresponds

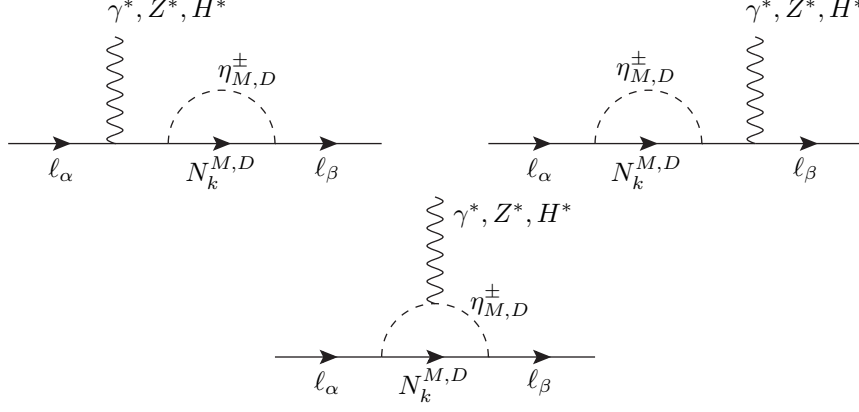


Figure 1: Feynman diagrams of the sub-processes which lead to the decay $\ell_\alpha \rightarrow \ell_\beta \ell_\delta \bar{\ell}_\delta$ and also the process $\mu N \rightarrow eN$. In these diagrams, the wavy line corresponds to off-shell photon, Z or Higgs boson. On the other hand, if the wavy line corresponds to on-shell photon, these diagrams lead to the decay $\ell_\alpha \rightarrow \ell_\beta \gamma$. The loops in these diagrams are driven by N_k^M and η_M^\pm (N_k^D and η_D^\pm) in the MSM(DSM).

to either photon, Z or Higgs boson. Now, by connecting the wavy line of Fig. 1 to a lepton and its anti-lepton will give rise to the 3-body decay $\ell_\alpha \rightarrow \ell_\beta \ell_\delta \bar{\ell}_\delta$. Moreover, by taking $\alpha = \mu$ and $\beta = e$ and connecting the wavy line of Fig. 1 to quarks would lead to $\mu \rightarrow e$ conversion in the presence of a nucleus N . As a result of the above given description, diagrams of Fig. 1 can be treated as sub-processes for the decay $\ell_\alpha \rightarrow \ell_\beta \ell_\delta \bar{\ell}_\delta$ and also for the $\mu N \rightarrow eN$ process. Notice that the diagrams of this figure give γ -, Z - and Higgs-penguin contributions to the decay $\ell_\alpha \rightarrow \ell_\beta \ell_\delta \bar{\ell}_\delta$ and also to the process $\mu N \rightarrow eN$. In the penguin contributions, the wavy line of Fig. 1 should represent an off-shell particle. On the other hand, if the wavy line of Fig. 1 represents on-shell photon, diagrams of this figure generate the decay $\ell_\alpha \rightarrow \ell_\beta \gamma$. Now, as indicated in Fig. 1, the loops in this figure are driven by either the fields of MSM or DSM, depending on the model under consideration. As a result of this, notice that the amplitudes of the above described LFV processes in the MSM are related to the corresponding amplitudes of the DSM, by interchanging the loop propagators and vertex couplings in the amplitudes. Hence, if the couplings and the masses of propagating fields have similar values in the MSM and DSM, the contributions to LFV processes are same in these two models.

Apart from the penguin contributions, 3-body decays which are of the form $\ell_\alpha \rightarrow \ell_\beta \bar{\ell}_\rho \bar{\ell}_\delta$ get additional contribution due to box diagrams. These are given in Fig. 2. Notice that there is no clash of arrows on the fermion propagator in the loop of the left-

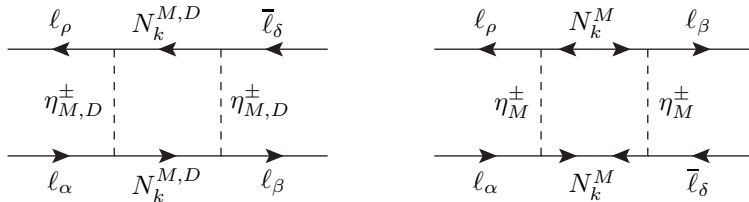


Figure 2: Box diagrams which lead to the decay $\ell_\alpha \rightarrow \ell_\beta \bar{\ell}_\rho \bar{\ell}_\delta$. The left-hand side diagram is possible in both the MSM and DSM, whereas, the right-hand side diagram is possible only in the MSM. Interchanging ℓ_β with ℓ_ρ in these diagrams give additional diagrams for the above decay.

hand side diagram of this figure. Hence, this diagram is possible in both the MSM and DSM. Also notice that, the amplitude of this diagram is the same in the MSM and DSM by interchanging the loop propagators and vertex couplings. In contrast to the above diagram, the right-hand side diagram of Fig. 1 is possible only in the MSM. Hence, we see that, the box diagrams give different contributions to the decay $\ell_\alpha \rightarrow \ell_\beta \bar{\ell}_\rho \bar{\ell}_\delta$ in the MSM and DSM. Essentially, the 3-body decays in the MSM get additional contribution in comparison to that of DSM. This result is in contrast to the penguin contributions to the LFV processes, which is discussed in the previous paragraph. Hence, it is likely that the MSM and DSM are distinguished through LFV processes, by searching the decays of the form $\ell_\alpha \rightarrow \ell_\beta \bar{\ell}_\rho \bar{\ell}_\delta$ in experiments.

In general, in the charged lepton sector, a 3-body decay is of the form $\ell_\alpha \rightarrow \ell_\beta \bar{\ell}_\rho \bar{\ell}_\delta$. Decays of this form can be categorized into: (i) $\ell_\alpha \rightarrow \ell_\beta \bar{\ell}_\beta \bar{\ell}_\beta$, (ii) $\ell_\tau \rightarrow \ell_\beta \bar{\ell}_\delta \bar{\ell}_\delta$, (iii) $\ell_\tau \rightarrow \ell_\beta \bar{\ell}_\beta \bar{\ell}_\delta$. Here, α can be either μ or τ and $\alpha \neq \beta \neq \delta$. β, δ can take either e or μ . Decays which are the forms $\ell_\alpha \rightarrow \ell_\beta \bar{\ell}_\beta \bar{\ell}_\beta$ and $\ell_\tau \rightarrow \ell_\beta \bar{\ell}_\delta \bar{\ell}_\delta$, are driven by diagrams of Figs. 1 and 2. On the other hand, decays of the form $\ell_\tau \rightarrow \ell_\beta \bar{\ell}_\beta \bar{\ell}_\delta$ take place only through the diagrams of Fig. 2. The above statements are true in both the MSM and DSM.

4 Analytical expressions in the MSM

In this section, we present analytical expressions for LFV processes in the MSM. In the next section, we present the corresponding expressions in the DSM. Before we proceed

further, below we describe the methodology in obtaining the analytical expressions. As stated before, the 3-body decays $\ell_\alpha \rightarrow \ell_\beta \ell_\rho \bar{\ell}_\delta$ may distinguish the MSM and DSM. Nevertheless, we compute the branching ratio for $\ell_\alpha \rightarrow \ell_\beta \gamma$ and also the conversion rate for $\mu N \rightarrow e N$. This is because, experimental limits on the processes $\mu \rightarrow e \gamma$ and $\mu N \rightarrow e N$ are stringent and they need to be included in the analysis of the LFV processes in the above two models. Now, while computing the analytical expressions for the above mentioned LFV processes, we first compute the amplitude of the decay $\ell_\alpha \rightarrow \ell_\beta \ell_\rho \bar{\ell}_\delta$. While doing this computation, we evaluate the penguin contribution, which is due to the diagrams of Fig. 1. Now, using the penguin contribution we compute the amplitudes for $\ell_\alpha \rightarrow \ell_\beta \gamma$ and $\mu N \rightarrow e N$ processes.

4.1 Branching ratio of $\ell_\alpha \rightarrow \ell_\beta \ell_\beta \bar{\ell}_\beta$

As described previously, the decay $\ell_\alpha \rightarrow \ell_\beta \ell_\beta \bar{\ell}_\beta$ gets contribution due to diagrams of Figs. 1 and 2. Below we describe the penguin contribution of Fig. 1 to the above decay and later we present the box contribution of Fig. 2 to this decay. Now, the amplitude due to γ -penguin diagrams to the decay $\ell_\alpha(p_1) \rightarrow \ell_\beta(p_2) \ell_\beta(p_3) \bar{\ell}_\beta(p_4)$ is

$$iM_\gamma(\ell_\alpha \rightarrow \ell_\beta \ell_\beta \bar{\ell}_\beta) = -\frac{e}{(p_1 - p_2)^2} \bar{u}(p_3) \gamma_\mu v(p_4) iM_{\ell_\alpha \rightarrow \ell_\beta \gamma^*}^\mu - (p_2 \leftrightarrow p_3) \quad (16)$$

Here, $M_{\ell_\alpha \rightarrow \ell_\beta \gamma^*}^\mu$ denotes the amplitude of the sub-process $\ell_\alpha \rightarrow \ell_\beta \gamma^*$. This amplitude is the resultant of the sum of the contributions of the diagrams of Fig. 1. Each of these diagrams give a divergent quantity. However, these divergences cancel out after summing the contributions of these diagrams. In the next paragraph, we describe the method [76] we have used for getting a finite amplitude from the diagrams of Fig. 1.

We assign momenta p_1 , p and p_2 to ℓ_α , N_k^M and ℓ_β , respectively, in the diagrams of Fig. 1. We define the following quantities, which appear in the propagators of the loops of Fig. 1.

$$D_k = p^2 - M_k^2, \quad D_{1\eta} = (p - p_1)^2 - m_{\eta_M^\pm}^2, \quad D_{2\eta} = (p - p_2)^2 - m_{\eta_M^\pm}^2 \quad (17)$$

Now, we define $b_{1,2}^k$, $c_{1,2}^k$, $d_{1,2}^k$, f^k and u^k through the following integrals [76]:

$$\begin{aligned} \int \frac{d^d p}{(2\pi)^d} \frac{p^\mu}{D_k D_{1\eta}} &= b_1^k p_1^\mu, & \int \frac{d^d p}{(2\pi)^d} \frac{p^\mu}{D_k D_{2\eta}} &= b_2^k p_2^\mu, \\ \int \frac{d^d p}{(2\pi)^d} \frac{p^\mu}{D_k D_{1\eta} D_{2\eta}} &= c_1^k p_1^\mu + c_2^k p_2^\mu, \\ \int \frac{d^d p}{(2\pi)^d} \frac{p^\mu p^\nu}{D_k D_{1\eta} D_{2\eta}} &= d_1^k p_1^\mu p_1^\nu + d_2^k p_2^\mu p_2^\nu + f^k (p_1^\mu p_2^\nu + p_2^\mu p_1^\nu) + u^k g^{\mu\nu} \end{aligned} \quad (18)$$

Notice that the above integrals appear in the amplitudes of the diagrams of Fig. 1. Here, the dimension d is taken to be 4, after the end of loop calculations. Using dimensional arguments, we see that $b_{1,2}^k$ and u^k are divergent quantities, whereas $c_{1,2}^k$, $d_{1,2}^k$ and f^k are finite. Now, using the integrals of Eq. (18), we obtain the following relations [76]:

$$b_1^k - b_2^k = q^2(d_1^k - d_2^k) + (m_{\ell_\alpha}^2 - m_{\ell_\beta}^2)(\kappa_1^k + \kappa_2^k), \quad (19)$$

$$m_{\ell_\alpha}^2 b_1^k - m_{\ell_\beta}^2 b_2^k = q^2(m_{\ell_\alpha}^2 d_1^k - m_{\ell_\beta}^2 d_2^k) + (m_{\ell_\alpha}^2 - m_{\ell_\beta}^2)[2u^k - q^2 f^k + m_{\ell_\alpha}^2 \kappa_1^k + m_{\ell_\beta}^2 \kappa_2^k], \quad (20)$$

$$\kappa_1^k = d_1^k + f^k - c_1^k, \quad \kappa_2^k = d_2^k + f^k - c_2^k \quad (21)$$

Here, $q = p_1 - p_2$. As stated before, in the integrals of Eq. (18), $b_{1,2}^k$ and u^k are divergent quantities and $c_{1,2}^k$, $d_{1,2}^k$ and f^k are finite. Since these integrals appear in the amplitudes of the diagrams of Fig. 1, after using the relations Eqs. (19) and (20) and after summing the contributions of these diagrams, we notice that divergences cancel out. As a result of this, after summing the contributions of these diagrams, the amplitude depends on the finite quantities $c_{1,2}^k$, $d_{1,2}^k$ and f^k . Below we give expressions for these quantities, which can be found by using Eq. (18). While obtaining these expressions, we neglect the masses of charged leptons. Hence, we have found

$$\begin{aligned} c^k = c_1^k = c_2^k &= \frac{-i}{16\pi^2} \int_0^1 dx \int_0^{1-x} dy \frac{y}{xM_K^2 + (1-x)m_{\eta_M^\pm}^2} \\ d^k = d_1^k = d_2^k &= \frac{-i}{16\pi^2} \int_0^1 dx \int_0^{1-x} dy \frac{y^2}{xM_K^2 + (1-x)m_{\eta_M^\pm}^2} \\ f^k &= \frac{-i}{16\pi^2} \int_0^1 dx \int_0^{1-x} dy \frac{y(1-x-y)}{xM_K^2 + (1-x)m_{\eta_M^\pm}^2} \end{aligned} \quad (22)$$

Since $c_1^k = c_2^k$ and $d_1^k = d_2^k$, we get $\kappa_1^k = \kappa_2^k = \kappa^k$. The description given above in this paragraph is applicable irrespective of the wavy line of Fig. 1 corresponds to γ^* , Z^* or H^* .

Let the wavy line of Fig. 1 be off-shell γ . Now, after using the description of the

previous paragraph, we have found the amplitude for the sub-process $\ell_\alpha \rightarrow \ell_\beta \gamma^*$ as

$$\begin{aligned}
iM_{\ell_\alpha \rightarrow \ell_\beta \gamma^*}^\mu &= ie\bar{u}(p_2)[A_1^{(\alpha,\beta)}q^2\gamma^\mu P_L + A_2^{(\alpha,\beta)}(m_{\ell_\alpha}P_R + m_{\ell_\beta}P_L)i\sigma^{\mu\nu}q_\nu \\
&\quad - A_1^{(\alpha,\beta)}(m_{\ell_\alpha}P_R - m_{\ell_\beta}P_L)q^\mu]u(p_1), \\
A_1^{(\alpha,\beta)} &= \sum_{k=1}^3 f_{\alpha k}^M f_{\beta k}^{M*} (-i)(d^k - f^k) = -\sum_{k=1}^3 f_{\alpha k}^M f_{\beta k}^{M*} \frac{1}{16\pi^2} \frac{1}{6m_{\eta_M^\pm}^2} G_1(x_k), \\
A_2^{(\alpha,\beta)} &= -\sum_{k=1}^3 f_{\alpha k}^M f_{\beta k}^{M*} (-i)\kappa^k = -\sum_{k=1}^3 f_{\alpha k}^M f_{\beta k}^{M*} \frac{1}{16\pi^2} \frac{1}{2m_{\eta_M^\pm}^2} G_2(x_k), \\
x_k &= \frac{M_k^2}{m_{\eta_M^\pm}^2}, \\
G_1(x) &= \frac{1}{6(1-x)^4} [2 - 9x + 18x^2 - 11x^3 + 6x^3 \ln x], \\
G_2(x) &= \frac{1}{6(1-x)^4} [1 - 6x + 3x^2 + 2x^3 - 6x^2 \ln x] \tag{23}
\end{aligned}$$

Here, $q = p_1 - p_2$, which is the momentum transfer in γ^* . m_{ℓ_α} is the mass of charged lepton ℓ_α . $P_{L,R} = \frac{1 \mp \gamma_5}{2}$. Notice that, $M_{\ell_\alpha \rightarrow \ell_\beta \gamma^*}^\mu$ satisfies the Ward identity $q_\mu M_{\ell_\alpha \rightarrow \ell_\beta \gamma^*}^\mu = 0$. After substituting the above amplitude in Eq. (16), we get the amplitude for the decay $\ell_\alpha \rightarrow \ell_\beta \ell_\beta \bar{\ell}_\beta$ due to the γ -penguin diagrams.

Above, we have described the calculations which lead to the amplitude for $\ell_\alpha \rightarrow \ell_\beta \ell_\beta \bar{\ell}_\beta$ due to the γ -penguin diagrams. In analogy to this, we compute the amplitude for the above decay due to the Z -penguin diagrams. This amplitude is given below, after neglecting the charged lepton masses.

$$iM_Z(\ell_\alpha \rightarrow \ell_\beta \ell_\beta \bar{\ell}_\beta) = \frac{g}{\cos \theta_W m_Z^2} \bar{u}(p_3) \gamma_\mu \left(\frac{1}{2} P_L - \sin^2 \theta_W \right) v(p_4) iM_{\ell_\alpha \rightarrow \ell_\beta Z^*}^\mu - (p_2 \leftrightarrow p_3) \tag{24}$$

Here, g is the $SU(2)_L$ gauge coupling, θ_W is the weak mixing angle and m_Z is the mass of Z gauge boson. $M_{\ell_\alpha \rightarrow \ell_\beta Z^*}^\mu$ denotes the amplitude for the sub-process $\ell_\alpha(p_1) \rightarrow \ell_\beta(p_2) Z^*(q)$, whose form is given below.

$$\begin{aligned}
iM_{\ell_\alpha \rightarrow \ell_\beta Z^*}^\mu &= i \frac{g}{\cos \theta_W} \bar{u}(p_2) \left[\left(\frac{1}{2} - \sin^2 \theta_W \right) A_1^{(\alpha,\beta)} q^2 \gamma^\mu P_L + A_2^{(\alpha,\beta)} m_{\ell_\alpha} m_{\ell_\beta} \gamma^\mu P_R \right. \\
&\quad \left. + \left(\frac{1}{2} - \sin^2 \theta_W \right) A_2^{(\alpha,\beta)} (m_{\ell_\alpha} P_R + m_{\ell_\beta} P_L) i\sigma^{\mu\nu} q_\nu \right. \\
&\quad \left. - \left(\frac{1}{2} - \sin^2 \theta_W \right) A_1^{(\alpha,\beta)} (m_{\ell_\alpha} P_R - m_{\ell_\beta} P_L) q^\mu \right] u(p_1) \tag{25}
\end{aligned}$$

See that the above amplitude and that in Eq. (23) have similar forms. Because of this similarity, the amplitude in Eq. (24) is suppressed in comparison to that of Eq. (16), due

to Z boson propagator mass. As a result of this, we have neglected the contribution due to Z -penguin diagrams in the computation of branching ratio of $\ell_\alpha \rightarrow \ell_\beta \ell_\beta \bar{\ell}_\beta$.

In analogy to the above given description, we can compute the amplitude to $\ell_\alpha \rightarrow \ell_\beta \ell_\beta \bar{\ell}_\beta$ due to Higgs-penguin diagrams, by taking the wavy line of Fig. 1 as off-shell Higgs boson. We expect this amplitude be sub-dominant due to the following reasons. First, in the Higgs-penguin diagrams, the Higgs boson always connects to either $\ell_e \bar{\ell}_e$ or $\ell_\mu \bar{\ell}_\mu$, whose coupling strength is very small in comparison to that of gauge coupling. Second, in the amplitude, we expect to get propagator suppression due to Higgs boson mass, which is in analogy to what we have found for Z -penguin diagrams. Because of the above two reasons, we neglect the contribution due to Higgs-penguin diagrams to the decay $\ell_\alpha \rightarrow \ell_\beta \ell_\beta \bar{\ell}_\beta$.

After computing the penguin contributions, we now describe the box contributions to $\ell_\alpha \rightarrow \ell_\beta \ell_\beta \bar{\ell}_\beta$. As stated previously, diagrams of Fig. 2 give box contributions, which are finite. The amplitude due to these contributions to the above decay is

$$\begin{aligned}
iM_{\text{box}}(\ell_\alpha \rightarrow \ell_\beta \ell_\beta \bar{\ell}_\beta) &= ie^2 B_\alpha^{(\beta, \beta, \bar{\beta})} \bar{u}(p_3) \gamma^\mu P_L v(p_4) \bar{u}(p_2) \gamma_\mu P_L u(p_1) \\
e^2 B_\alpha^{(\beta, \beta, \bar{\beta})} &= B_{1\alpha}^{(\beta, \beta, \bar{\beta})} + B_{2\alpha}^{(\beta, \beta, \bar{\beta})}, \\
B_{1\alpha}^{(\beta, \beta, \bar{\beta})} &= -\frac{1}{16\pi^2 m_\pm^2} \sum_{\eta_M^\pm, n, k=1}^3 f_{\alpha n}^M f_{\beta n}^{M*} f_{\beta k}^M f_{\beta k}^{M*} D_1(x_n, x_k) \\
B_{2\alpha}^{(\beta, \beta, \bar{\beta})} &= \frac{1}{16\pi^2 m_\pm^2} \sum_{\eta_M^\pm, n, k=1}^3 f_{\alpha n}^M f_{\beta n}^M f_{\beta k}^{M*} f_{\beta k}^{M*} \sqrt{x_n x_k} D_2(x_n, x_k) \\
D_1(x, y) &= \frac{1}{2(1-x)(1-y)} + \frac{x^2 \ln x}{2(1-x)^2(x-y)} + \frac{y^2 \ln y}{2(1-y)^2(y-x)} \\
D_2(x, y) &= -\frac{1}{(1-x)(1-y)} - \frac{x \ln x}{(1-x)^2(x-y)} - \frac{y \ln y}{(1-y)^2(y-x)} \quad (26)
\end{aligned}$$

Here, $B_{1\alpha}^{(\beta, \beta, \bar{\beta})}$ and $B_{2\alpha}^{(\beta, \beta, \bar{\beta})}$ are the contributions arising due to left- and right-hand side diagrams of Fig. 2, respectively.

We have described the amplitudes arising due to penguin and box diagrams to the decay $\ell_\alpha \rightarrow \ell_\beta \ell_\beta \bar{\ell}_\beta$. As stated above, we are neglecting contributions due to Z - and Higgs-penguin diagrams. Now, after squaring the above described amplitudes, we get the branching ratio for the decay $\ell_\alpha \rightarrow \ell_\beta \ell_\beta \bar{\ell}_\beta$, which is

$$\begin{aligned}
\text{Br}(\ell_\alpha \rightarrow \ell_\beta \ell_\beta \bar{\ell}_\beta) &= \frac{3(4\pi\alpha_{em})^2}{8G_F^2} \left\{ \frac{1}{6} |B_\alpha^{(\beta, \beta, \bar{\beta})}|^2 + |A_1^{(\alpha, \beta)}|^2 + |A_2^{(\alpha, \beta)}|^2 \left(\frac{16}{3} \ln \frac{m_{\ell_\alpha}}{2m_{\ell_\beta}} - \frac{26}{9} \right) \right. \\
&\quad \left. + \left[-\frac{1}{3} B_\alpha^{(\beta, \beta, \bar{\beta})} (A_1^{(\alpha, \beta)})^* + \frac{2}{3} B_\alpha^{(\beta, \beta, \bar{\beta})} (A_2^{(\alpha, \beta)})^* - 2A_1^{(\alpha, \beta)} (A_2^{(\alpha, \beta)})^* + h.c. \right] \right\} \\
&\quad \times \text{Br}(\ell_\alpha \rightarrow \ell_\beta \nu_\alpha \bar{\nu}_\beta) \quad (27)
\end{aligned}$$

Here, $\alpha_{em} = \frac{e^2}{4\pi}$ and G_F is the Fermi constant.

In Sec. 1, we have stated that, in the MSM, study on the LFV processes have previously been done in [73]. Here we compare the analytical results we have obtained for $\ell_\alpha \rightarrow \ell_\beta \ell_\beta \bar{\ell}_\beta$ in comparison to that of [73]. We notice that the expressions for the amplitudes we have given in Eqs. (16) and (26) agree with the corresponding expressions of [73]. In fact, the dipole and non-dipole contributions, which are given in [73], have an overall minus sign in comparison to that of ours. But otherwise, the form of these contributions agree with that of ours. However, we have found some discrepancy in the amplitude of Eq. (24) with the corresponding expression of [73]. Nevertheless, we have argued that Z -penguin diagrams give sub-dominant contribution to the decay $\ell_\alpha \rightarrow \ell_\beta \ell_\beta \bar{\ell}_\beta$, which is also the case in [73]. As a result of this, we expect that, our analytical expressions for $\ell_\alpha \rightarrow \ell_\beta \ell_\beta \bar{\ell}_\beta$ agree with that of [73]. Indeed, the branching ratio of this decay, which is given in Eq. (27), agrees with the corresponding expression of [73], apart from a minor difference in the term multiplying $|A_2^{(\alpha,\beta)}|^2$.

In the numerical analysis, which we present in Sec. 6, we denote the decay $\ell_\alpha \rightarrow \ell_\beta \ell_\beta \bar{\ell}_\beta$ as $\ell_\alpha \rightarrow 3\ell_\beta$, for the sake of simplicity.

4.2 Branching ratio of $\ell_\tau \rightarrow \ell_\beta \ell_\delta \bar{\ell}_\delta$

The decay $\ell_\tau \rightarrow \ell_\beta \ell_\delta \bar{\ell}_\delta$ gets contribution due to both penguin and box diagrams. Computation of these contributions to the above decay is analogous to what we have presented in the previous subsection. Now, the amplitude to the decay $\ell_\tau(p_1) \rightarrow \ell_\beta(p_2) \ell_\delta(p_3) \bar{\ell}_\delta(p_4)$ due to γ -penguin diagrams is

$$iM_\gamma(\ell_\tau \rightarrow \ell_\beta \ell_\delta \bar{\ell}_\delta) = -\frac{e}{(p_1 - p_2)^2} \bar{u}(p_3) \gamma_\mu v(p_4) iM_{\ell_\tau \rightarrow \ell_\beta \gamma^*}^\mu \quad (28)$$

Here, $M_{\ell_\tau \rightarrow \ell_\beta \gamma^*}^\mu$ is the amplitude for the sub-process $\ell_\tau \rightarrow \ell_\beta \gamma^*$, which can be found from $M_{\ell_\alpha \rightarrow \ell_\beta \gamma^*}^\mu$ by putting $\alpha = \tau$ in Eq. (23). Now, the amplitude to the above decay due to Z -penguin contribution can be analogously found from Eqs. (24) and (25). However, notice that this contribution is sub-dominant due to propagator suppression of Z boson mass. Hence, this contribution is neglected in the rest of the calculations. Similarly, the Higgs-penguin contribution is also neglected for the above decay, due to the reasons presented in the previous subsection. Now, the amplitude due to box diagrams of Fig. 2

to the above decay is given by

$$\begin{aligned}
iM_{\text{box}}(\ell_\tau \rightarrow \ell_\beta \ell_\delta \bar{\ell}_\delta) &= ie^2 B_\tau^{(\beta, \delta, \bar{\delta})} \bar{u}(p_3) \gamma^\mu P_L v(p_4) \bar{u}(p_2) \gamma_\mu P_L u(p_1) \\
e^2 B_\tau^{(\beta, \delta, \bar{\delta})} &= B_{1\tau}^{(\beta, \delta, \bar{\delta})} + B_{2\tau}^{(\beta, \delta, \bar{\delta})}, \\
B_{1\tau}^{(\beta, \delta, \bar{\delta})} &= -\frac{1}{32\pi^2 m^2} \sum_{\eta_M^\pm} \sum_{n,k=1}^3 [f_{\tau n}^M f_{\beta n}^{M*} f_{\delta k}^M f_{\delta k}^{M*} + f_{\delta n}^M f_{\beta n}^{M*} f_{\tau k}^M f_{\delta k}^{M*}] D_1(x_n, x_k) \\
B_{2\tau}^{(\beta, \delta, \bar{\delta})} &= \frac{1}{16\pi^2 m^2} \sum_{\eta_M^\pm} \sum_{n,k=1}^3 f_{\tau n}^M f_{\delta n}^M f_{\delta k}^{M*} f_{\beta k}^{M*} \sqrt{x_n x_k} D_2(x_n, x_k) \quad (29)
\end{aligned}$$

Here again, $B_1^{(\beta, \delta)}$ and $B_2^{(\beta, \delta)}$ are the contributions arising due to left- and right-hand side diagrams of Fig. 2, respectively.

After squaring the amplitudes in Eqs. (28) and (29), we get branching ratio of the decay $\ell_\tau \rightarrow \ell_\beta \ell_\delta \bar{\ell}_\delta$, which is

$$\begin{aligned}
\text{Br}(\ell_\tau \rightarrow \ell_\beta \ell_\delta \bar{\ell}_\delta) &= \frac{3(4\pi\alpha_{em})^2}{8G_F^2} \left\{ \frac{1}{3} |B_\tau^{(\beta, \delta, \bar{\delta})}|^2 + \frac{2}{3} |A_1^{(\tau, \beta)}|^2 + |A_2^{(\tau, \beta)}|^2 \left(\frac{16}{3} \ln \frac{m_{\ell_\tau}}{2m_{\ell_\delta}} - \frac{32}{9} \right) \right. \\
&\quad \left. + \left[-\frac{1}{3} B_\tau^{(\beta, \delta, \bar{\delta})} (A_1^{(\tau, \beta)})^* + \frac{2}{3} B_\tau^{(\beta, \delta, \bar{\delta})} (A_2^{(\tau, \beta)})^* - \frac{4}{3} A_1^{(\tau, \beta)} (A_2^{(\tau, \beta)})^* + h.c. \right] \right\} \\
&\quad \times \text{Br}(\ell_\tau \rightarrow \ell_\beta \nu_\tau \bar{\nu}_\beta) \quad (30)
\end{aligned}$$

4.3 Branching ratio of $\ell_\tau \rightarrow \ell_\beta \ell_\beta \bar{\ell}_\delta$

The decay $\ell_\tau(p_1) \rightarrow \ell_\beta(p_2) \ell_\beta(p_3) \bar{\ell}_\delta(p_4)$ takes place only through the box diagrams of Fig. 2. The amplitude for this decay is

$$\begin{aligned}
iM_{\text{box}}(\ell_\tau \rightarrow \ell_\beta \ell_\beta \bar{\ell}_\delta) &= ie^2 B_\tau^{(\beta, \beta, \bar{\delta})} \bar{u}(p_3) \gamma^\mu P_L v(p_4) \bar{u}(p_2) \gamma_\mu P_L u(p_1) \\
e^2 B_\tau^{(\beta, \beta, \bar{\delta})} &= B_{1\tau}^{(\beta, \beta, \bar{\delta})} + B_{2\tau}^{(\beta, \beta, \bar{\delta})}, \\
B_{1\tau}^{(\beta, \beta, \bar{\delta})} &= -\frac{1}{16\pi^2 m^2} \sum_{\eta_M^\pm} \sum_{n,k=1}^3 f_{\tau n}^M f_{\beta n}^{M*} f_{\delta k}^M f_{\beta k}^{M*} D_1(x_n, x_k) \\
B_{2\tau}^{(\beta, \beta, \bar{\delta})} &= \frac{1}{16\pi^2 m^2} \sum_{\eta_M^\pm} \sum_{n,k=1}^3 f_{\tau n}^M f_{\delta n}^M f_{\beta k}^{M*} f_{\beta k}^{M*} \sqrt{x_n x_k} D_2(x_n, x_k) \quad (31)
\end{aligned}$$

After squaring this amplitude, the branching ratio of the above decay is

$$\text{Br}(\ell_\tau \rightarrow \ell_\beta \ell_\beta \bar{\ell}_\delta) = \frac{3(4\pi\alpha_{em})^2}{8G_F^2} \left\{ \frac{1}{6} |B_\tau^{(\beta, \beta, \bar{\delta})}|^2 \right\} \times \text{Br}(\ell_\tau \rightarrow \ell_\beta \nu_\tau \bar{\nu}_\beta) \quad (32)$$

4.4 Branching ratio of $\ell_\alpha \rightarrow \ell_\beta \gamma$

Previously, we have described the amplitude for the process $\ell_\alpha \rightarrow \ell_\beta \gamma^*$ in Eq. (23). By taking γ to be on-shell in this process, one can read out the amplitude for $\ell_\alpha(p_1) \rightarrow$

$\ell_\beta(p_2)\gamma(q)$, which is given below.

$$iM(\ell_\alpha \rightarrow \ell_\beta\gamma) = ie\bar{u}(p_2)A_2^{(\alpha,\beta)}(m_{\ell_\alpha}P_R + m_{\ell_\beta}P_L)i\sigma^{\mu\nu}q_\nu\epsilon_\mu(q)u(p_1) \quad (33)$$

After squaring this amplitude, we get the branching ratio for the above decay, which is

$$\text{Br}(\ell_\alpha \rightarrow \ell_\beta\gamma) = \frac{48\pi^3\alpha_{em}}{G_F^2}|A_2^{(\alpha,\beta)}|^2\text{Br}(\ell_\alpha \rightarrow \ell_\beta\nu_\alpha\bar{\nu}_\beta) \quad (34)$$

The above branching ratio formula agrees with the corresponding formula, which is originally given in [77].

4.5 Conversion rate of $\mu \rightarrow e$ in a nucleus

As described in Sec. 3, $\mu \rightarrow e$ conversion in a nucleus takes place through the penguin diagrams of Fig. 1, by attaching the wavy line of this figure to a quark field. Now, analogous to the arguments given for the case of 3-body decays, we expect γ -penguin diagrams to give dominant contribution to the $\mu \rightarrow e$ conversion, since the Z - and Higgs-penguin diagrams have propagator suppressions. The theory for computing conversion rate of $\mu \rightarrow e$ in a nucleus is described in [78]. The analytical expression for this conversion rate is [78]

$$\begin{aligned} \text{CR}(\mu \rightarrow e, \text{Nucleus}) &= \frac{p_e E_e m_\mu^3 G_F^2 \alpha_{em}^3 Z_{eff}^4 F_p^2}{8\pi^2 Z} \\ &\times \left\{ |(Z+N)(g_{LV}^{(0)} + g_{LS}^{(0)}) + (Z-N)(g_{LV}^{(1)} + g_{LS}^{(1)})|^2 \right. \\ &\quad \left. + |(Z+N)(g_{RV}^{(0)} + g_{RS}^{(0)}) + (Z-N)(g_{RV}^{(1)} + g_{RS}^{(1)})|^2 \right\} \frac{1}{\Gamma_{\text{capt}}} \quad (35) \end{aligned}$$

Here, p_e and E_e are the momentum and energy of the electron. Z_{eff} and F_p are the effective atomic charge and nuclear matrix element, whose definitions can be found in [78]. Γ_{capt} is the total muon capture rate. Z and N are the number of protons and neutrons in the nucleus. The quantities $g_{XK}^{(0)}$ and $g_{XK}^{(1)}$, where $X = L, R$ and $K = S, V$, are isoscalar and isovector couplings, respectively. These couplings arise due to mediation of either scalar or vector field between quarks and the effective $\mu - e$ vertex. Numerical values for the quantities p_e , Z_{eff} , F_p and Γ_{capt} can be found in [79–81] for various nuclei. To compute the couplings $g_{XK}^{(0)}$ and $g_{XK}^{(1)}$, we have followed [82]. Below, we briefly describe the computation of these couplings. The effective $\mu - e$ vertex, in our work, is generated by the diagrams of Fig. 1. Since we have argued that Higgs-penguin diagrams give sub-dominant contribution, we have taken $g_{XS}^{(0)} = 0 = g_{XS}^{(1)}$. We have also neglected the contribution

due to Z -penguin diagrams in the effective $\mu - e$ vertex. Now, the amplitude due to γ -penguin diagrams is given in Eq. (23), which gives a parametrization to the effective $\gamma\mu e$ vertex. Notice that the term containing q^μ in Eq. (23) does not contribute to the $\mu \rightarrow e$ conversion at the quark level. Now, following the procedure described in [82], we have found

$$\begin{aligned} g_{LV}^{(0)} = g_{LV}^{(1)} &= \frac{4\pi\alpha_{em}}{\sqrt{2}G_F} (A_1^{(\mu,e)} - A_2^{(\mu,e)}) \\ g_{RV}^{(0)} = g_{RV}^{(1)} &= -\frac{4\pi\alpha_{em}}{\sqrt{2}G_F} \frac{m_{\ell_e}}{m_{\ell_\mu}} A_2^{(\mu,e)} \end{aligned} \quad (36)$$

5 Analytical expressions in the DSM

In Sec. 3, we have described the Feynman diagrams which induce the LFV processes in the MSM and DSM. We have explained that the amplitudes of LFV processes in the DSM can be found from the corresponding expressions of the MSM, by replacing the vertex couplings and propagator masses accordingly. As a result of this, in the case of LFV processes $\ell_\alpha \rightarrow \ell_\beta\gamma$ and $\mu \rightarrow e$ conversion, the analytical expressions presented in Secs. 4.4 and 4.5 are valid for the DSM, by making the following replacements in these expressions:

$$f_{\alpha k}^M \rightarrow f_{k\alpha}^D, \quad m_{\eta_{\pm}^M}^2 \rightarrow m_{\eta_{\pm}^D}^2, \quad M_k \rightarrow M'_k \quad (37)$$

Now, for the case of 3-body LFV decays, it is explained in Sec. 3 that the decays in the MSM get additional contribution due to right-hand side diagram of Fig. 2. As a result of this, while obtaining analytical expressions for 3-body LFV decays in the DSM, one should discard the contributions of $B_{2\alpha}^{(\beta,\beta,\bar{\beta})}$, $B_{2\tau}^{(\beta,\delta,\bar{\delta})}$ and $B_{2\tau}^{(\beta,\beta,\bar{\delta})}$, which are presented in Secs. 4.1, 4.2 and 4.3, respectively. Now, after doing this, the analytical expressions presented in Secs. 4.1, 4.2 and 4.3 are applicable for the case of DSM, by making the replacements of Eq. (37).

6 Numerical analysis

After presenting analytical expressions in the previous two sections, here we present numerical analysis of the LFV processes in both the MSM and DSM. Among all the LFV processes, which are listed in Tab. 1, the most stringent experimental limits are obtained on $\text{Br}(\mu \rightarrow e\gamma)$, $\text{Br}(\mu \rightarrow 3e)$ and $\text{CR}(\mu \rightarrow e, \text{Au})$. Hence, we first do an analysis on

the above three observables and study which of these observables can give dominant constraints on the parameter space of the MSM and DSM. While doing the above analysis, we have found that the perturbativity of Yukawa couplings play a major role. The above analysis is relevant in work, since the experimental limits on the above three observables need to be satisfied while doing the analysis on the LFV τ decays.

As mentioned previously, studies on LFV processes in the MSM and DSM have been done in [56, 73]. Below we describe the difference between our analysis, which is described in the previous paragraph, and that of [56, 73]. In [73], it is studied under what conditions $\text{Br}(\mu \rightarrow 3e)$ and $\text{CR}(\mu \rightarrow e, \text{Au})$ can exceed over $\text{Br}(\mu \rightarrow e\gamma)$, by considering specific benchmark points of the parameter space of the MSM. Notice that the experimental limits on $\text{Br}(\mu \rightarrow e\gamma)$, $\text{Br}(\mu \rightarrow 3e)$ and $\text{CR}(\mu \rightarrow e, \text{Au})$ are different. Hence, it is more reasonable to study the following question: if the experimental limit on $\text{Br}(\mu \rightarrow e\gamma)$ is satisfied, is there any parameter space where $\text{Br}(\mu \rightarrow 3e)$ and $\text{CR}(\mu \rightarrow e, \text{Au})$ can exceed over the experimental limits on these observables? The above question is addressed in this work by considering the role of perturbativity of Yukawa couplings. In [73], perturbativity bounds on Yukawa couplings are satisfied in the analysis. However, the role of these perturbativity bounds is not discussed. On the other hand, in [56], where the model is closely related to the DSM, a correlation between $\text{Br}(\mu \rightarrow e\gamma)$ and $\text{Br}(\mu \rightarrow 3e)$ is studied. However, our analysis is more general than that of [56].

As stated before, perturbativity bounds on Yukawa couplings play a major role in the analysis of LFV in the MSM and DSM. In order that the Yukawa couplings to be within the perturbative bounds, we should have

$$|f_{\alpha k}^M| \leq \sqrt{4\pi}, \quad |f_{k\alpha}^D| \leq \sqrt{4\pi} \quad (38)$$

in both the MSM and DSM, respectively. The expressions for f^M and f^D , in the case of our analysis, have been given in Eqs. (8) and (15), respectively. We see that the magnitudes of the elements of U_{PMNS} are less than $\mathcal{O}(1)$. As a result of this, we define the following quantity

$$\text{PER}_{M(D)} = \text{Max} \left[\sqrt{\frac{m_1}{4\pi|\Lambda_1^{M(D)}|}}, \sqrt{\frac{m_2}{4\pi|\Lambda_2^{M(D)}|}}, \sqrt{\frac{m_3}{4\pi|\Lambda_3^{M(D)}|}} \right] \quad (39)$$

We now see that, if $\text{PER}_M \leq 1$ and $\text{PER}_D \leq 1$ are satisfied in the analysis of the MSM and DSM, respectively, the perturbativity bounds of Eq. (38) are satisfied in the respective models. We describe the role of PER_M and PER_D in our analysis later.

The Yukawa couplings f^M and f^D depend on neutrino masses and mixing angles, which are found from the neutrino oscillation data. From the global fits to neutrino oscillation data, the following mass-square differences among the neutrino fields are found [65].

$$m_s^2 = m_2^2 - m_1^2 = 7.5 \times 10^{-5} \text{ eV}^2, \quad m_a^2 = \begin{cases} m_3^2 - m_1^2 = 2.55 \times 10^{-3} \text{ eV}^2 & (\text{NO}) \\ m_1^2 - m_3^2 = 2.45 \times 10^{-3} \text{ eV}^2 & (\text{IO}) \end{cases}. \quad (40)$$

Here, NO(IO) represents normal(inverted) ordering. In the above equation, we have given the best fit values. In order to fit the above mass-square differences, we take the neutrino mass eigenvalues as

$$\begin{aligned} \text{NO : } & m_1 \lesssim m_s, \quad m_2 = \sqrt{m_s^2 + m_1^2}, \quad m_3 = \sqrt{m_a^2 + m_1^2}. \\ \text{IO : } & m_3 \lesssim m_s, \quad m_1 = \sqrt{m_a^2 + m_3^2}, \quad m_2 = \sqrt{m_s^2 + m_1^2}. \end{aligned} \quad (41)$$

Notice that the lightest neutrino mass in NO and IO is still undetermined. Hence, in our analysis, we have varied the lightest neutrino mass in the range $[0, m_s]$. Also, in our analysis, we have applied the cosmological upper bound on the sum of neutrino masses, which is 0.12 eV [3]. Apart from the neutrino masses, neutrino mixing angles and CP violating Dirac phase are also found from the global fits to neutrino oscillation data [65]. The best fit and 3σ ranges for these variables are given in Tab. 4. Notice that, in the case

parameter	best fit	3σ range
$\sin^2 \theta_{12}/10^{-1}$	3.18	2.71 - 3.69
$\sin^2 \theta_{13}/10^{-2}$ (NO)	2.200	2.000 - 2.405
$\sin^2 \theta_{13}/10^{-2}$ (IO)	2.225	2.018 - 2.424
$\sin^2 \theta_{23}/10^{-1}$ (NO)	5.74	4.34 - 6.10
$\sin^2 \theta_{23}/10^{-1}$ (IO)	5.78	4.33 - 6.08
δ_{CP}/o (NO)	194	128 - 359
δ_{CP}/o (IO)	284	200 - 353

Table 4: Best fit and 3σ ranges for the neutrino mixing angles and CP violating Dirac phase, which are obtained from the global fits to neutrino oscillation data [65].

of MSM, the Yukawa couplings f^M can depend on two Majorana phases through U_{PMNS} . However, these Majorana phases are not determined in experiments so far. Hence, we have taken these phases to be zero in our analysis.

6.1 Numerical results in the MSM

We first present results on the following observables: $\text{Br}(\mu \rightarrow e\gamma)$, $\text{Br}(\mu \rightarrow 3e)$, $\text{CR}(\mu \rightarrow e, \text{Au})$. Among these observables, the experimental limit on $\text{Br}(\mu \rightarrow e\gamma)$ is more stringent. Hence, in our analysis, after satisfying the experimental limit on $\text{Br}(\mu \rightarrow e\gamma)$, we compute the quantities $\text{Br}(\mu \rightarrow 3e)$ and $\text{CR}(\mu \rightarrow e, \text{Au})$. The above analysis is done after scanning over the parameter space of the MSM. It is to remind that the above observables depend on the masses of the fields η_M^\pm and N_k^M , which drive these LFV processes at 1-loop level, whose discussion is presented in Sec. 3. Apart from the above mentioned fields, the above observables depend on the Yukawa couplings, which are determined by the neutrino oscillation observables and also by the masses of neutral fields η_{MR} and η_{MI} . Previously, we have described about the neutrino oscillation observables of neutrino masses and mixing angles. In our analysis, we have varied the neutrino mixing angles and δ_{CP} over the allowed 3σ ranges, which are given in Tab. 4. As for the neutrino masses, we have varied them according to the description given around Eq. (41). Now, the masses of the fields η_M^\pm , η_{MR} , η_{MI} and N_k^M can be expressed in terms of $m_{\eta_M^\pm}^2$, λ_4 , λ_5 and M_k . In this analysis, we have taken N_k^M to be non-degenerate and parameterized their masses as M_1 , $M_1 + \delta_M$, $M_1 + 2\delta_M$. Here, δ_M give mass splitting between two N_k^M fields. The parameter λ_4 is varied in the range $[-4\pi, 4\pi]$. Later, we specifically mention the ranges for $m_{\eta_M^\pm}^2$ and λ_5 . However, we have varied the above parameters in such a way that the following bounds are satisfied on the masses of η_{MR} and η_{MI} :

$$m_R \geq 5 \text{ GeV}, \quad m_I \geq 5 \text{ GeV} \quad (42)$$

Above, we have described the methodology of our scanning procedure. In this procedure, after satisfying the experimental bound on $\text{Br}(\mu \rightarrow e\gamma)$, we have computed $\text{Br}(\mu \rightarrow 3e)$ and $\text{CR}(\mu \rightarrow e, \text{Au})$. These results are presented in Fig. 3 for the case of NO. In this figure, we have fixed $m_{\eta_M^\pm} = 500 \text{ GeV}$ and $\delta_M = 1 \text{ TeV}$. We have varied M_1 and λ_5 in the ranges $[10, 100] \text{ TeV}$ and $[10^{-11}, 10^{-10}]$, respectively. From the left-hand side plot of Fig. 3, we see that the blue points are allowed from the constraints of both perturbativity of Yukawa couplings and experimental bound of $\text{Br}(\mu \rightarrow 3e)$. The green points in this plot are disallowed due to violating the perturbativity bounds on the Yukawa couplings. Notice that some of these green points also violate the experimental bound on $\text{Br}(\mu \rightarrow 3e)$. On the other hand, the red points in the above mentioned plot, satisfy the perturbativity bound on Yukawa couplings but violate the experimental bound on $\text{Br}(\mu \rightarrow 3e)$. From the right-hand side plot of Fig. 3, we see that the values of $\text{CR}(\mu \rightarrow e, \text{Au})$ are within the experimental bound on this observable, even if the

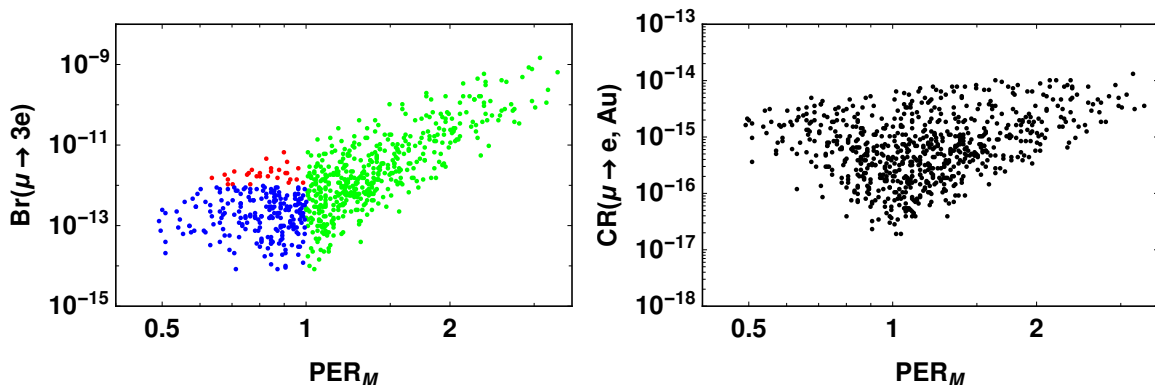


Figure 3: $\text{Br}(\mu \rightarrow 3e)$ and $\text{CR}(\mu \rightarrow e, \text{Au})$ versus PER_M , after satisfying the experimental bound on $\text{Br}(\mu \rightarrow e\gamma)$. The plots are for the case of NO and $m_{\eta_M^\pm} < M_1$. The color coding in the left-hand side plot is as follows: green points violate the perturbativity bound on the Yukawa couplings, red points violate the experimental bound on $\text{Br}(\mu \rightarrow 3e)$, blue points are allowed by the above mentioned bounds. See text, for more details.

perturbativity bound on the Yukawa couplings is violated. What this implies is that if the experimental bound on $\text{Br}(\mu \rightarrow e\gamma)$ is satisfied, the observable $\text{CR}(\mu \rightarrow e, \text{Au})$ may not give further constraints on the parametric space of the model. On the other hand, $\text{Br}(\mu \rightarrow 3e)$ can impose additional constraints on the parametric space. Notice that, in addition to $\text{Br}(\mu \rightarrow 3e)$, PER_M gives a significant constraint on the parametric space, which is evident from the left-hand side plot of Fig. 3.

Plots in Fig. 3 are illustrative to show the role of PER_M , $\text{Br}(\mu \rightarrow 3e)$ and $\text{CR}(\mu \rightarrow e, \text{Au})$ in constraining the parametric space of the model, in addition to the constraints imposed by $\text{Br}(\mu \rightarrow e\gamma)$. In this figure, we have taken specific values for $m_{\eta_M^\pm}$ and δ_M , and specific ranges for M_1 and λ_5 . Below we describe what happens if we vary one of the above quantities and keeping the others same as in Fig. 3. We have varied $m_{\eta_M^\pm}$ to 1 TeV in the plots of Fig. 3 and we have found the plots remain qualitatively same. Similarly, after varying δ_M , the plots in Fig. 3 have remained qualitatively same. The values of M_1 in Fig. 3 are large compared to that of $m_{\eta_M^\pm}$. If we decrease M_1 less than 10 TeV in Fig. 3, we have found PER_M to be less than 1. In this case, we get very few number of points which violate the experimental bound on $\text{Br}(\mu \rightarrow 3e)$ in addition to the points which satisfy this experimental bound. On the other hand, by increasing M_1 more than 100 TeV in Fig. 3, PER_M is found to be larger than 1. This case can be completely ruled out by solely imposing constraints of $\text{Br}(\mu \rightarrow e\gamma)$ and PER_M . Lastly, by varying λ_5 to be below 10^{-11} in Fig. 3, PER_M is to found to be greater than 1. Hence, this

case is completely ruled out with the constraints of $\text{Br}(\mu \rightarrow e\gamma)$ and PER_M . Now, by varying λ_5 to be above 10^{-10} in Fig. 3, we have found PER_M to be less than 1 and all the points would satisfy the constraint on $\text{Br}(\mu \rightarrow 3e)$. In all the above described cases, we have found the values of $\text{CR}(\mu \rightarrow e, \text{Au})$ to be below the experimental bound on this observable.

Notice that PER_M is inversely related to Λ_k^M , which in turn is inversely related to either $m_{\eta_M^\pm}$ or M_k . Hence, PER_M increases with M_k . On the other hand, $\Lambda_k^M \rightarrow 0$ in the limit $\lambda_5 \rightarrow 0$. Hence, by decreasing λ_5 , PER_M increases. The above described features supplement the description given in the previous paragraph.

From the plots of Fig. 3, we have noticed that, among the different LFV observables, $\text{Br}(\mu \rightarrow e\gamma)$ and $\text{Br}(\mu \rightarrow 3e)$ can impose constraints on the parametric space of the model, if not by $\text{CR}(\mu \rightarrow e, \text{Au})$. We can understand this in the following way. Both the processes $\mu \rightarrow e\gamma$ and $\mu\text{Au} \rightarrow e\text{Au}$ are driven by the diagrams of Fig. 1. Hence, after making naive order of estimation in the expressions of $\text{Br}(\mu \rightarrow e\gamma)$ and $\text{CR}(\mu \rightarrow e, \text{Au})$, one can arrive at $\text{CR}(\mu \rightarrow e, \text{Au}) < \text{Br}(\mu \rightarrow e\gamma)$ for any parametric point in the model. Since the experimental bound on $\text{Br}(\mu \rightarrow e\gamma)$ is stringent than that on $\text{CR}(\mu \rightarrow e, \text{Au})$, $\text{CR}(\mu \rightarrow e, \text{Au})$ may not give additional constraints on the model if the bound on $\text{Br}(\mu \rightarrow e\gamma)$ is satisfied. On the other hand, for the process $\mu \rightarrow 3e$, box diagrams of Fig. 2 contribute, in addition to the diagrams of Fig. 1. Notice that the amplitudes of box diagrams are proportional to quartic in Yukawa couplings, whereas, the amplitudes of diagrams of Fig. 1 vary as quadratic in Yukawa couplings. Hence, for large values of Yukawa couplings, the contribution of box diagrams can overcome that of Fig. 1. Indeed, from the left-hand side plot of Fig. 3, we see that for $\text{PER}_M \gtrsim 1$, $\text{Br}(\mu \rightarrow 3e)$ can exceed over the experimental bound on it. We have noticed that in the region of $\text{PER}_M \sim 1$, contribution from box diagrams in $\text{Br}(\mu \rightarrow 3e)$ is dominant. Hence, for large Yukawa couplings, $\text{Br}(\mu \rightarrow 3e)$ can give additional constraints on the model parameters in addition to that from $\text{Br}(\mu \rightarrow e\gamma)$.

Results about $\text{Br}(\mu \rightarrow 3e)$ and $\text{CR}(\mu \rightarrow e, \text{Au})$, in the case of IO, are presented in Fig. 4, after satisfying the experimental bound on $\text{Br}(\mu \rightarrow e\gamma)$. In this figure, the values of $m_{\eta_M^\pm}$ and δ_M are same as that in Fig. 3. Moreover, the ranges of M_1 and λ_5 are same as that in Fig. 3. From the left-hand side plot of Fig. 4, we see that the whole parametric region is ruled out either with the perturbativity bound on Yukawa couplings or by the experimental bound on $\text{Br}(\mu \rightarrow 3e)$. On the other hand, from the right-hand side of this figure, notice that $\text{CR}(\mu \rightarrow e, \text{Au})$ is not giving any additional constraints on the parametric region. Plots in this figure are illustrative to show the role played by $\text{Br}(\mu \rightarrow 3e)$ and PER_M in giving constraints on the model parameters, in addition to the

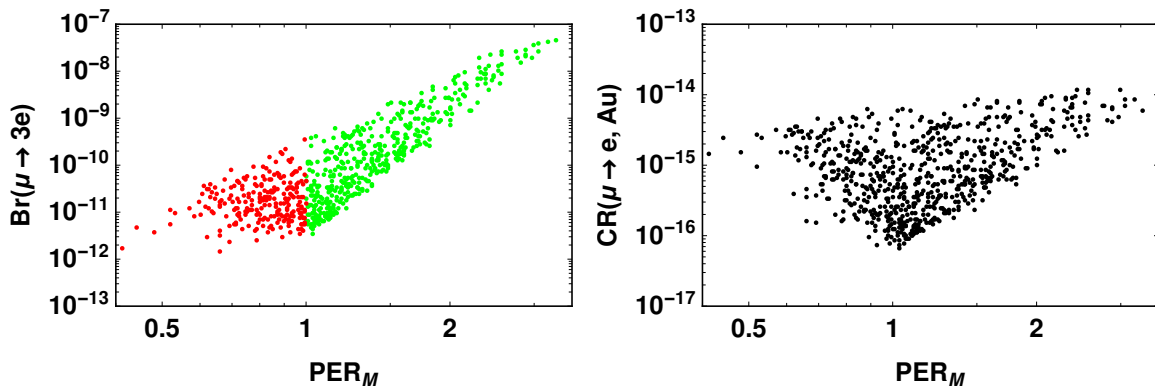


Figure 4: $\text{Br}(\mu \rightarrow 3e)$ and $\text{CR}(\mu \rightarrow e, \text{Au})$ versus PER_M , after satisfying the experimental bound on $\text{Br}(\mu \rightarrow e\gamma)$. The plots are for the case of IO and $m_{\eta_M^\pm} < M_1$. The color coding in the left-hand side plot is same as that in Fig. 3. See text, for more details.

constraints imposed by $\text{Br}(\mu \rightarrow e\gamma)$. After comparing the plots of this figure with that of Fig. 3, notice that $\text{Br}(\mu \rightarrow 3e)$ and $\text{CR}(\mu \rightarrow e, \text{Au})$ are enhanced in the case of IO as compared to that of NO. The reason for this enhancement is that, in the case of IO, the neutrino mass eigenvalues are large as compared to that in NO. As a result of this, the Yukawa couplings are large in the case of IO as compared to that of NO.

In Figs. 3 and 4, we have explained that $\text{Br}(\mu \rightarrow 3e)$ can give additional constraints on the parametric space, even if $\text{PER}_M < 1$ and $\text{Br}(\mu \rightarrow e\gamma) < 3.1 \times 10^{-13}$. However, these plots are made for the case of $m_{\eta_M^\pm} < M_1$. We have done the above mentioned analysis for the case $m_{\eta_M^\pm} > M_1$. Now, in this case and for NO, we have not found a parametric space where $\text{Br}(\mu \rightarrow 3e)$ can give additional constraints if $\text{PER}_M < 1$ and $\text{Br}(\mu \rightarrow e\gamma) < 3.1 \times 10^{-13}$. On the other hand, in the case of IO and for $m_{\eta_M^\pm} > M_1$, we have found a region where $\text{Br}(\mu \rightarrow 3e)$ can give additional constraints in addition to that of PER_M and $\text{Br}(\mu \rightarrow e\gamma)$. These results are presented in Fig. 5. In this figure we have taken $M_1 = 1$ TeV and $\delta_M = 500$ GeV. We have varied $m_{\eta_M^\pm}$ and λ_5 in the ranges $[10, 100]$ TeV and $[10^{-9}, 10^{-8}]$, respectively. From the left-hand side plot of this figure, we see that red points indicate the region where $\text{Br}(\mu \rightarrow 3e)$ give additional constraints even if $\text{PER}_M < 1$ and $\text{Br}(\mu \rightarrow e\gamma) < 3.1 \times 10^{-13}$. From the right-hand side plot of this figure, notice that $\text{CR}(\mu \rightarrow e, \text{Au})$ does not give additional constraint.

In Figs. 3–5, we have shown how parameter space of the MSM can be constrained by PER_M , $\text{Br}(\mu \rightarrow e\gamma)$, $\text{Br}(\mu \rightarrow 3e)$ and $\text{CR}(\mu \rightarrow e, \text{Au})$. By applying the constraints due to above mentioned quantities, we have obtained branching ratios of the LFV tau decays. These results are presented in Fig. 6 for the case of NO. Notice that, we have described

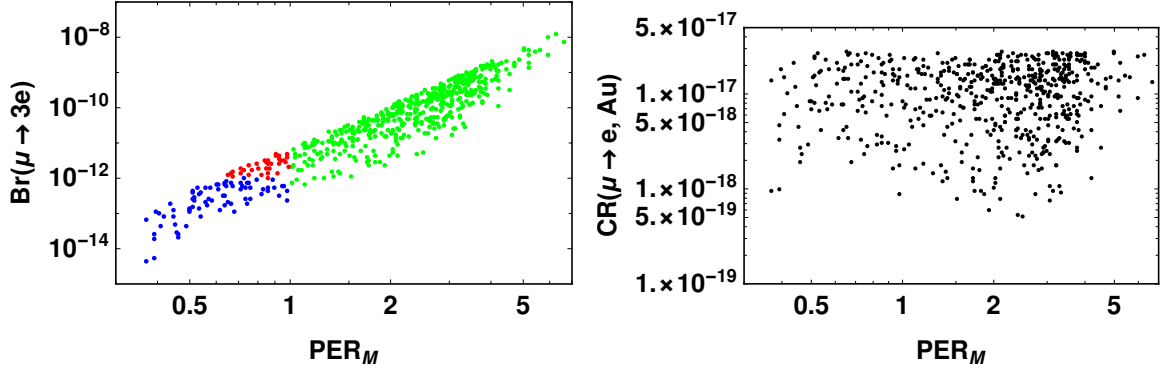


Figure 5: $\text{Br}(\mu \rightarrow 3e)$ and $\text{CR}(\mu \rightarrow e, \text{Au})$ versus PER_M , after satisfying the experimental bound on $\text{Br}(\mu \rightarrow e\gamma)$. The plots are for the case of IO and $m_{\eta_M^\pm} > M_1$. The color coding in the left-hand side plot is same as that in Fig. 3. See text, for more details.

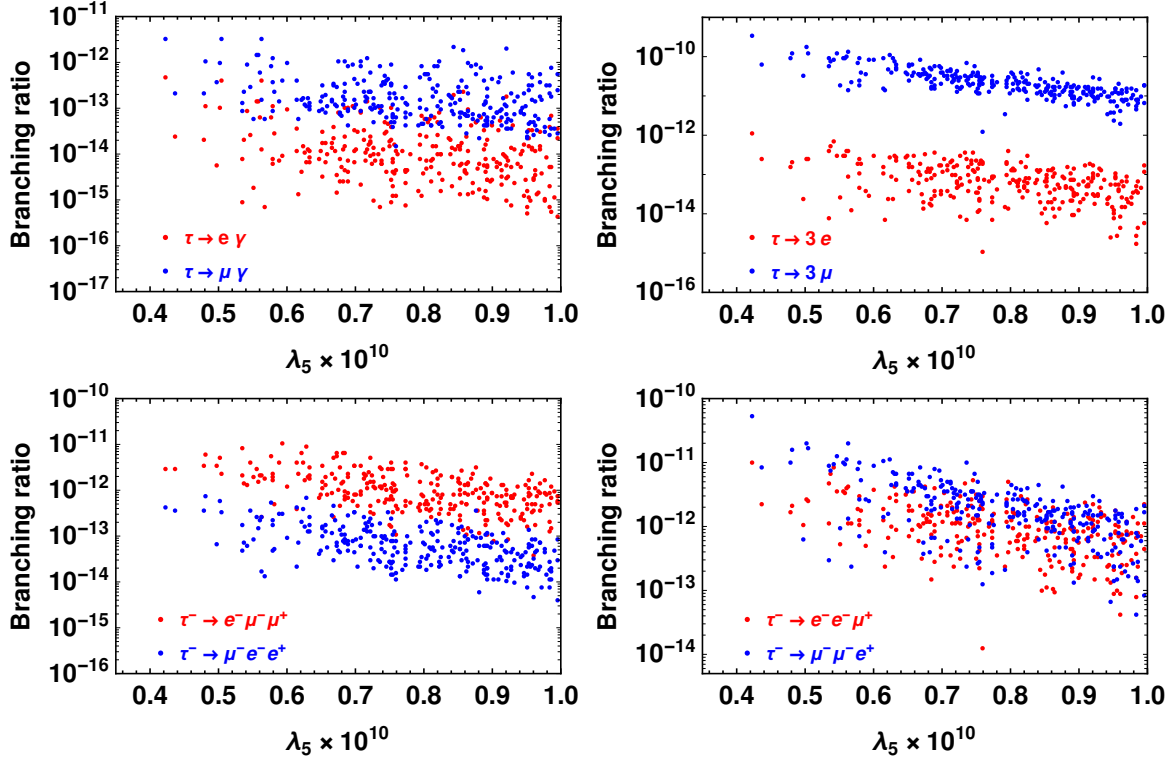


Figure 6: Branching ratios of various LFV tau decays in the MSM and for the case of NO, after applying the constraints due to PER_M , $\text{Br}(\mu \rightarrow e\gamma)$, $\text{Br}(\mu \rightarrow 3e)$ and $\text{CR}(\mu \rightarrow e, \text{Au})$. See text, for more details.

before that $\text{CR}(\mu \rightarrow e, \text{Au})$ is not giving additional constraints on the model parameters. However, for the sake of completeness we have satisfied the experimental upper bound on $\text{CR}(\mu \rightarrow e, \text{Au})$ in Fig. 6. In this figure, we have fixed $\delta_M = 1$ TeV. We have varied

$m_{\eta_M^\pm}$ and M_1 in the ranges $[100, 1000]$ GeV and $[5, 50]$ TeV, respectively, in this figure. For the above mentioned ranges, we have found that the branching ratios in this figure to be maximal. Notice that $\text{Br}(\tau \rightarrow 3\mu)$ can reach the maximum as around 10^{-10} . This value is two orders less than the current experimental bound on $\text{Br}(\tau \rightarrow 3\mu)$. In future experiments, this decay branching ratio will be probed to a sensitivity of $\sim 10^{-11} - 10^{-10}$ [83, 84]. Hence, the MSM can be tested in the future experiments in the decay channel $\tau \rightarrow 3\mu$. The other LFV tau decays in the MSM can reach the maximum as around $10^{-13} - 10^{-11}$. These values are three to four orders less than the current experimental bounds on these decays. In Fig. 6, notice that λ_5 should be $\gtrsim 4 \times 10^{-11}$. In our scan, the value of λ_5 is restricted by the constraints due to PER_M , $\text{Br}(\mu \rightarrow e\gamma)$, $\text{Br}(\mu \rightarrow 3e)$ and $\text{CR}(\mu \rightarrow e, \text{Au})$. Indeed, in our scan, if we vary $m_{\eta_M^\pm}$ and M_1 independently over the range $[100, 10^5]$ GeV, we have found λ_5 is restricted to be $\gtrsim \times 10^{-11}$. Since the values of λ_5 given in Fig. 6 are the lowest allowed values, we see that the Yukawa couplings should be large for these values, whose statement is explained in Sec. 2.1. As a result of the above discussion, we expect the branching ratios of LFV tau decays to be maximal. In fact, this statement is vindicated in our analysis, where we have found that, when $\text{PER}_M \sim 1$ the branching ratios of LFV tau decays are becoming maximal.

We have obtained analog plots of Fig. 6, for the case of IO. These results are presented in Fig. 7. In this figure, we have fixed $\delta_M = 1$ TeV. We have varied $m_{\eta_M^\pm}$ and M_1 independently in the range $[.5, 50]$ TeV. For the above mentioned range, we have found the branching ratios in this figure to be maximal. From this figure, we notice that the branching ratio of $\tau^- \rightarrow e^- e^- \mu^+$ can reach as around 10^{-11} . The branching ratio of other LFV tau decays can reach as around $10^{-13} - 10^{-12}$. Notice that the maximal values of branching ratios of the decays $\tau \rightarrow e\gamma$, $\tau \rightarrow \mu\gamma$, $\tau^- \rightarrow \mu^- e^- e^+$ and $\tau^- \rightarrow e^- e^- \mu^+$ in Fig. 7 are nearly same as that of the corresponding decays in Fig. 6. On the other hand, for the rest of the LFV tau decays, the maximal values of the branching ratios in Fig. 7 are suppressed as compared to that of the corresponding decays in Fig. 6. This implies that we can test the LFV tau decays in future experiments in the case of NO rather than that for the case of IO. The value of λ_5 in Fig. 7 is restricted by the constraints due to PER_M , $\text{Br}(\mu \rightarrow e\gamma)$, $\text{Br}(\mu \rightarrow 3e)$ and $\text{CR}(\mu \rightarrow e, \text{Au})$. From this figure, we see that the λ_5 should be $\gtrsim 10^{-10}$. Notice that the allowed value of λ_5 , in the case of IO, is larger than that for the case of NO. As a result of this, we expect the magnitude of allowed Yukawa couplings in the case of IO to be lower than that for the case of NO. This may be a reason for why the maximal values of branching ratios of LFV tau decays in the case of IO are unable to exceed than that for the case of NO.

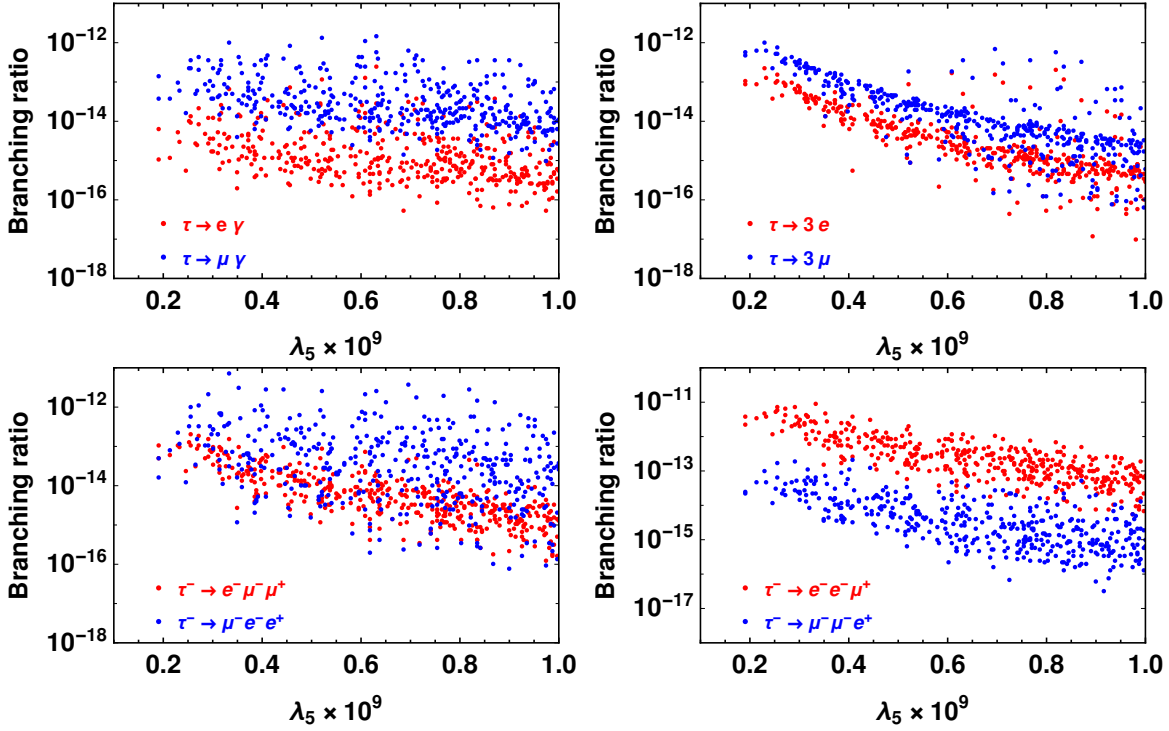


Figure 7: Branching ratios of various LFV tau decays in the MSM and for the case of IO, after applying the constraints due to PER_M , $\text{Br}(\mu \rightarrow e\gamma)$, $\text{Br}(\mu \rightarrow 3e)$ and $\text{CR}(\mu \rightarrow e, \text{Au})$. See text, for more details.

6.2 Numerical results in the DSM

In analogy to the results presented in the previous subsection, here, we first present results on the observables $\text{Br}(\mu \rightarrow e\gamma)$, $\text{Br}(\mu \rightarrow 3e)$ and $\text{CR}(\mu \rightarrow e, \text{Au})$. Below we describe our methodology of scanning procedure through which we determine the above observables in the DSM. The above observables, apart from the Yukawa couplings, depend on the masses of the fields η_D^\pm and N_k^D . Notice that the Yukawa couplings depend on the neutrino oscillation observables, masses of the fields N_k^D , $\zeta_{1,2}$ and the mixing parameter θ . As for the neutrino oscillation observables, we vary the neutrino mixing angles according to the 3σ ranges of Tab. 4 and the neutrino masses are varied according to the description given around Eq. (41). Now, the masses of the fields η_D^\pm , N_k^D , $\zeta_{1,2}$ and the mixing parameter θ can be parameterized in terms of the variables $m_{\eta_D^\pm}$, M'_k , m_χ , λ'_4 , λ'_5 and $\frac{A}{v}$. Here, M'_k indicate the mass of the fields N_k^D , which we have taken to be non-degenerate in our analysis. We have parameterized the masses of N_k^D as M'_1 , $M'_1 + \delta'_M$ and $M'_1 + 2\delta'_M$, where δ'_M give splitting in the masses. The parameters $\lambda'_{4,5}$ are varied independently over $[-4\pi, 4\pi]$. Later, in our analysis, we specify the values taken for the variables $m_{\eta_D^\pm}$, m_χ

and $\frac{A}{v}$. We have varied them in such a way that the following lower bounds are satisfied on the masses of $\zeta_{1,2}$:

$$m_{\zeta_1} \geq 5 \text{ GeV}, \quad m_{\zeta_2} \geq 5 \text{ GeV} \quad (43)$$

In our scanning procedure, we have computed the observables $\text{Br}(\mu \rightarrow 3e)$ and $\text{CR}(\mu \rightarrow e, \text{Au})$ after satisfying the experimental bound on $\text{Br}(\mu \rightarrow e\gamma)$. In our analysis we have found that $\text{CR}(\mu \rightarrow e, \text{Au})$ does not give additional constraints on the parameter space of the DSM. This result is analogous to that presented in the previous subsection for the case of MSM. The above result should not be surprising, since both DSM and MSM are similar to each other in terms of model perspective. Next, we have searched for $\text{Br}(\mu \rightarrow 3e)$ to give any additional constraints on the model parameters, after satisfying the experimental bound on $\text{Br}(\mu \rightarrow e\gamma)$ and also the perturbativity bound on the Yukawa couplings. The perturbativity bound of Yukawa couplings in the DSM is satisfied by imposing $\text{PER}_D < 1$. In our scanning analysis, in the case of NO, after imposing $\text{Br}(\mu \rightarrow e\gamma) < 3.1 \times 10^{-13}$ and $\text{PER}_D < 1$, we have found that $\text{Br}(\mu \rightarrow 3e)$ does not give additional constraints on the parameter space of the model. On the other hand, in the case of IO, $\text{Br}(\mu \rightarrow 3e)$ is found to give additional constraints on the model parameters. These results are presented in Fig. 8. The plots in this figure are illustrative, which are shown for various cases that differ in the values of $m_{\eta_D^\pm}$ and M'_1 . In the top-left plot of Fig. 8, we have fixed $m_{\eta_D^\pm} = 500 \text{ GeV}$ and $\delta'_M = 1 \text{ TeV}$. In this plot, we have varied M'_1 , m_χ and $\frac{A}{v}$ in the ranges $[10^4, 10^5] \text{ GeV}$, $[10, 10^5] \text{ GeV}$ and $[10^{-11}, 10^{-10}]$, respectively. Notice that this plot refers to the case of $m_{\eta_D^\pm} < M'_1$. In the top-right plot of Fig. 8, which corresponds to the case $m_{\eta_D^\pm} > M'_1$, we have fixed $M'_1 = 500 \text{ GeV}$ and $\delta'_M = 50 \text{ GeV}$. In this plot, we have varied $m_{\eta_D^\pm}$, m_χ and $\frac{A}{v}$ in the ranges $[10^4, 10^5] \text{ GeV}$, $[10, 10^5] \text{ GeV}$ and $[10^{-9}, 10^{-8}]$, respectively. Finally, in the bottom plot of Fig. 8, which represents the case $m_{\eta_D^\pm} \sim M'_1$, we have fixed $\delta'_M = 1 \text{ TeV}$ and varied $m_{\eta_D^\pm}$, M'_1 , m_χ and $\frac{A}{v}$ in the ranges $[10^4, 10^5] \text{ GeV}$, $[10^4, 10^5] \text{ GeV}$, $[10^3, 10^4] \text{ GeV}$ and $[10^{-10}, 10^{-9}]$, respectively. From the plots of Fig. 8, we see red points which indicate $\text{Br}(\mu \rightarrow 3e) > 10^{-12}$ and $\text{PER}_D < 1$. Essentially, these red points correspond to additional constraints due to $\text{Br}(\mu \rightarrow 3e)$, even after satisfying the constraints on $\text{Br}(\mu \rightarrow e\gamma)$ and PER_D . Notice that there are only few red points in Fig. 8 as compared to that in Figs. 3–5, which are for the case of MSM. This implies that the additional constraints due to $\text{Br}(\mu \rightarrow 3e)$ are not so severe in the DSM as compared to that in the MSM. The reason for this can be understood in the following way. As described in Sec. 6.1, the constraints due to $\text{Br}(\mu \rightarrow 3e)$ become severe in the limit that the Yukawa couplings becoming large. It is further explained that the

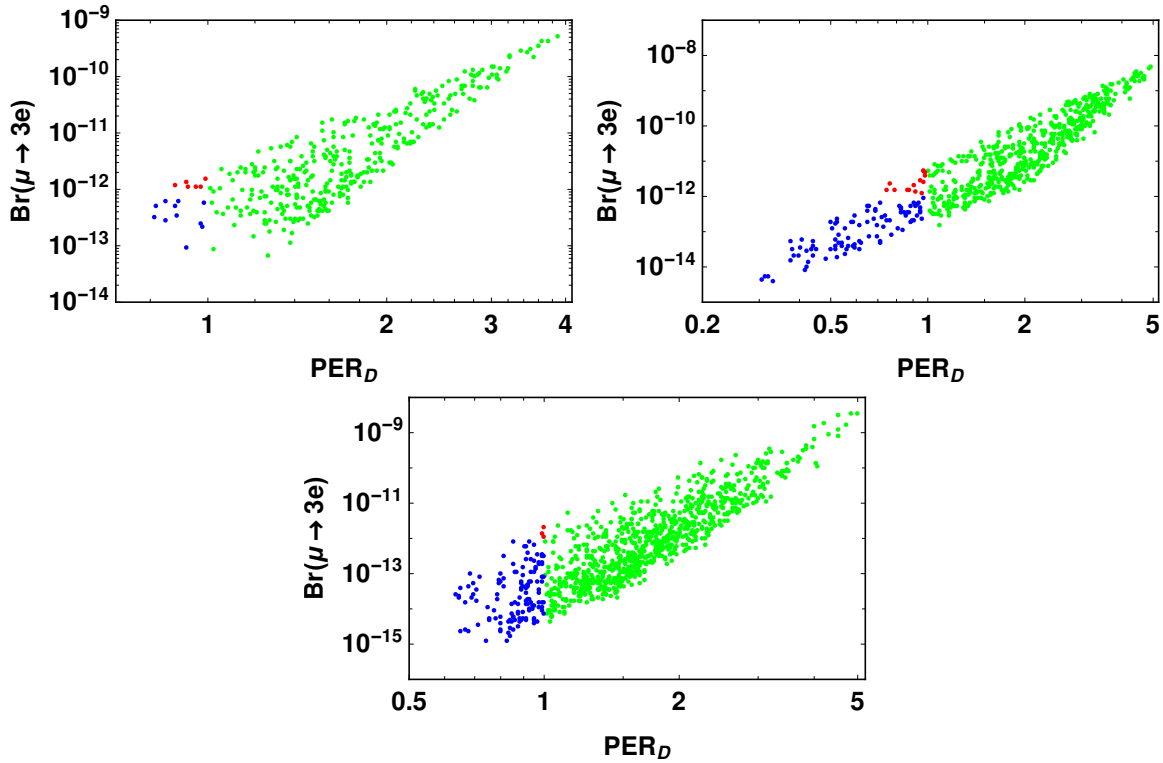


Figure 8: $\text{Br}(\mu \rightarrow 3e)$ versus PER_D , after satisfying the experimental bound on $\text{Br}(\mu \rightarrow e\gamma)$. The plots are for the case of IO. Top-left and -right plots are for the cases $m_{\eta_D^\pm} < M'_1$ and $m_{\eta_D^\pm} > M'_1$, respectively. The bottom plot is for the case $m_{\eta_D^\pm} \sim M'_1$. The color coding in these plots is same as that in Fig. 3. See text, for more details.

box diagrams of Fig. 2 give dominant contribution to $\text{Br}(\mu \rightarrow 3e)$ in the above mentioned limit. Now, it is evident that both the box diagrams of Fig. 2 contribute to the decay $\mu \rightarrow 3e$ in the MSM. Whereas, only the left-hand side diagram of Fig. 2 contribute to $\mu \rightarrow 3e$ in the DSM. Since more contribution due to box diagrams is possible in the MSM as against to that in the DSM, constraints due to $\text{Br}(\mu \rightarrow 3e)$ are more severe in the MSM as compared to that in the DSM.

In the previous paragraph, we have explained the constraints arising due to PER_D , $\text{Br}(\mu \rightarrow e\gamma)$, $\text{Br}(\mu \rightarrow 3e)$ and $\text{CR}(\mu \rightarrow e, \text{Au})$. After satisfying the constraints due to above mentioned quantities, we have computed the branching ratios of LFV tau decays in the DSM. These results are presented in Fig. 9. Although we have described before that $\text{CR}(\mu \rightarrow e, \text{Au})$ is not giving additional constraints on the model parameters, for the sake of completeness we have satisfied the experimental limit on this observable in Fig. 9. In this figure, we have fixed $\delta'_M = 1$ TeV and we have varied $m_{\eta_D^\pm}$, M'_1 and m_χ in the ranges $[5, 50]$ TeV, $[5, 50]$ GeV and $[50, 500]$ GeV, respectively. For the above mentioned ranges,

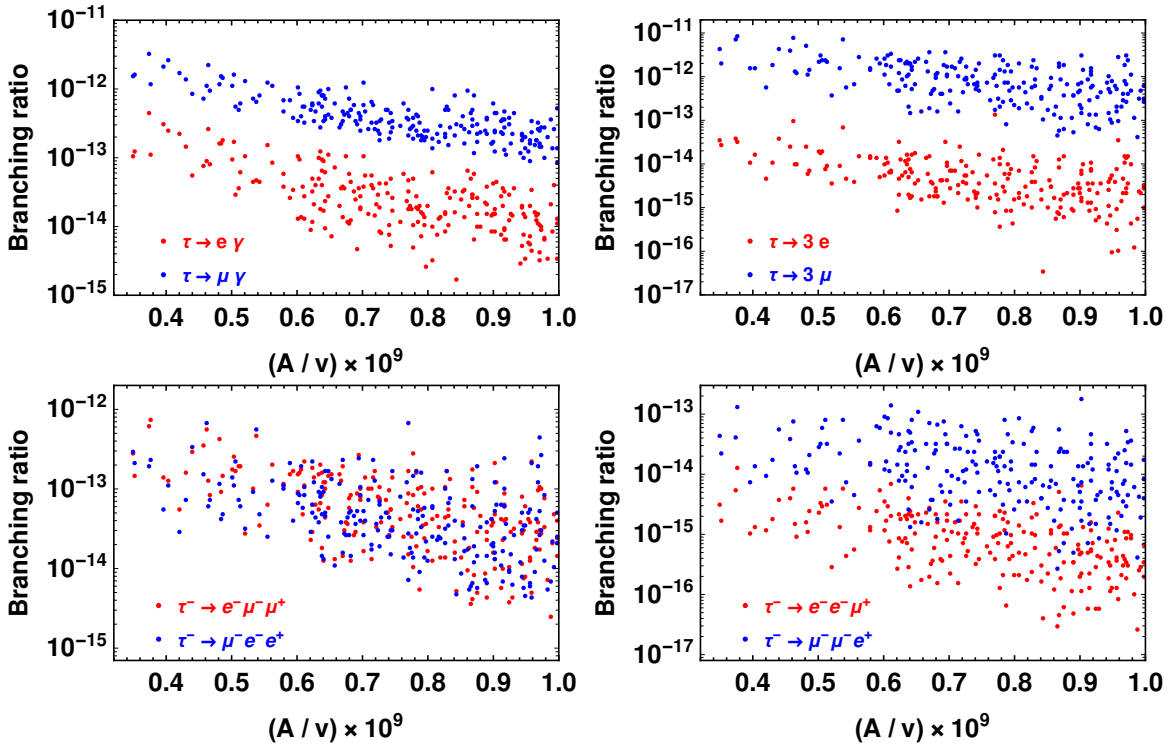


Figure 9: Branching ratios of various LFV tau decays in the DSM and for the case of NO, after applying the constraints due to PER_D , $\text{Br}(\mu \rightarrow e\gamma)$, $\text{Br}(\mu \rightarrow 3e)$ and $\text{CR}(\mu \rightarrow e, \text{Au})$. See text, for more details.

we have found that the branching ratios in this figure can reach maximum values. Among the various LFV tau decays, $\text{Br}(\tau \rightarrow 3\mu)$ can have a maximum value of around 10^{-11} . Although this value is three orders less than the current experimental limit on this decay, this value can be probed in the future experiments [83, 84]. The next best after $\tau \rightarrow 3\mu$ is the decay $\tau \rightarrow \mu\gamma$, whose branching ratio can reach a maximum of $\sim 10^{-12}$. Rest of the branching ratios of tau decays in Fig. 9 are further suppressed to be below 10^{-12} . Notice that the value of $\frac{A}{v}$ in Fig. 9 is restricted to be $\gtrsim 3.2 \times 10^{-10}$. This restriction is due to the constraints of PER_D , $\text{Br}(\mu \rightarrow e\gamma)$, $\text{Br}(\mu \rightarrow 3e)$ and $\text{CR}(\mu \rightarrow e, \text{Au})$. In fact, in our scanning analysis, we have found that $\frac{A}{v}$ is restricted to be larger than 10^{-10} even if we vary $m_{\eta_D^\pm}$, M'_1 and m_χ independently over a larger range of $[100, 10^5]$ GeV. Since the values of $\frac{A}{v}$ are the lowest possible in Fig. 9, the Yukawa couplings become large for these values, whose statement is explained in Sec. 2.2. As a result of this, we expect the branching ratios in Fig. 9 to become maximal. Explicitly, in our analysis, we have seen that the branching ratios in this figure reach maximum when $\text{PER}_D \sim 1$.

Below we compare the results of Fig. 9 with the analog results in the case of MSM,

which are presented in Fig. 7. Notice that the maximal reaches of $\text{Br}(\tau \rightarrow e\gamma)$ and $\text{Br}(\tau \rightarrow \mu\gamma)$ are nearly same in the DSM and MSM. On the other hand, for the rest of the LFV tau decays, which are 3-body decays, the maximal reaches of the branching ratios in the DSM are at least suppressed by an order one as compared to that in the MSM. For these 3-body LFV tau decays, the contribution comes from the penguin diagrams of Fig. 1 and also from the box diagrams of Fig. 2. As already explained before, the branching ratios of these decays become maximal when the Yukawa couplings are large, which implies that the contribution of box diagrams overcome that of dipole diagrams in these decays. Now, we know that two different box diagrams contribute for the above decays in the MSM as against to only one in the case of DSM. As a result of this, the maximal reaches in the branching ratios of the 3-body LFV tau decays are suppressed in the DSM as compared to that in the MSM. Now, as for the case of 2-body LFV decays $\tau \rightarrow e\gamma$ and $\tau \rightarrow \mu\gamma$, the contribution to these decays come only due to the penguin diagrams. Since the topology of penguin diagrams is same between the MSM and DSM, the maximal reaches in the branching ratios of the 2-body LFV tau decays remain to be nearly same in the MSM and DSM.

We have obtained the analog plots of Fig. 9 for the case of IO. These results are presented in Fig. 10. In this figure, we have fixed $\delta'_M = 1$ TeV and we have varied $m_{\eta_D^\pm}$, M'_1 and m_χ in the ranges $[5, 50]$ TeV, $[5, 50]$ TeV and $[50, 500]$ GeV, respectively. For the above mentioned ranges, we have found that the branching ratios in this figure can reach maximum values. In this figure, the value of $\frac{A}{v}$ is restricted due to the constraints of PER_D , $\text{Br}(\mu \rightarrow e\gamma)$, $\text{Br}(\mu \rightarrow 3e)$ and $\text{CR}(\mu \rightarrow e, \text{Au})$. The lowest allowed value of $\frac{A}{v}$ in this figure is nearly the same as that in Fig. 9. Notice that $\text{Br}(\tau \rightarrow \mu\gamma)$, $\text{Br}(\tau \rightarrow 3\mu)$ and $\text{Br}(\tau^- \rightarrow \mu^- e^- e^+)$ can reach maximum values of around 10^{-12} in Fig. 10. For the rest of the LFV tau decays in Fig. 10, the branching ratios are suppressed below 10^{-12} . After comparing the results in Fig. 10 with the analog results of Fig. 9, we see that the maximum values of LFV tau decays in the case of IO are unable to exceed over that of the corresponding decays in the case of NO, except for the decay $\tau^- \rightarrow \mu^- e^- e^+$. Again, we make the comparison between the results of Fig. 10 and the analog results in the MSM, which are presented in Fig. 8. We see that, in the case of IO, the maximal values of the branching ratios of LFV tau decays in the DSM are unable to overcome that of the corresponding decays in the MSM.

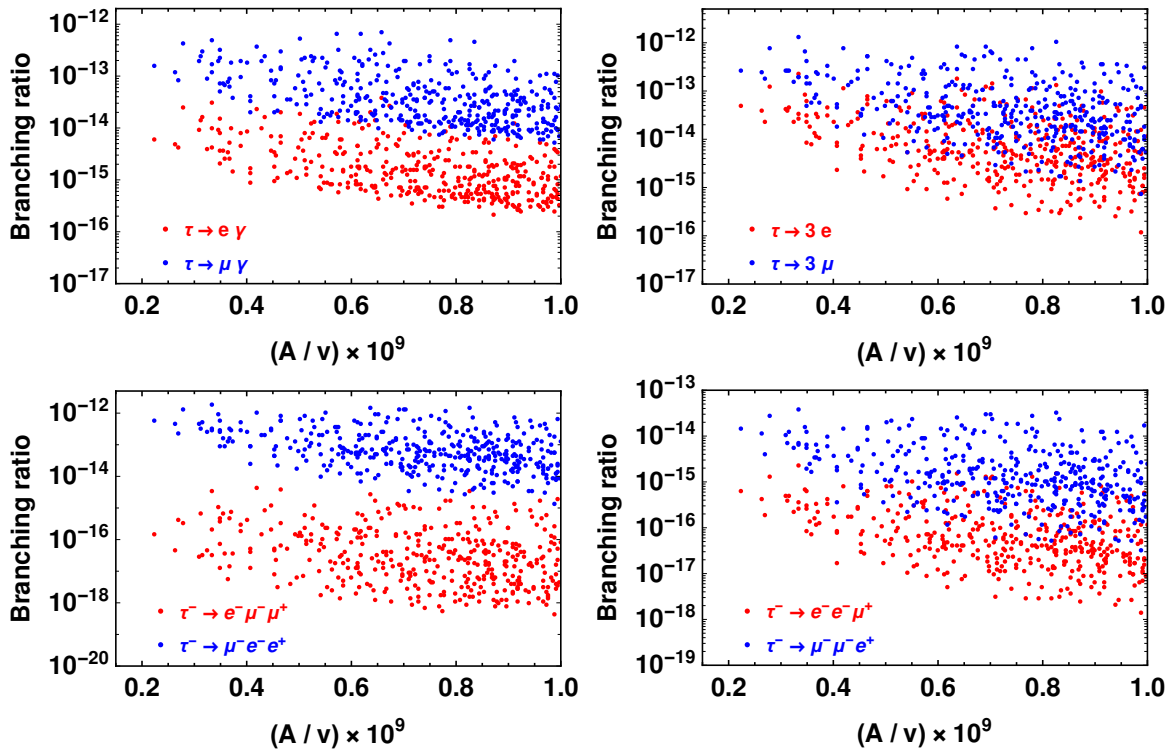


Figure 10: Branching ratios of various LFV tau decays in the DSM and for the case of IO, after applying the constraints due to PER_D , $\text{Br}(\mu \rightarrow e\gamma)$, $\text{Br}(\mu \rightarrow 3e)$ and $\text{CR}(\mu \rightarrow e, \text{Au})$. See text, for more details.

7 Conclusions

In this work, we have studied LFV processes in the charged lepton sector of the two minimal versions of the scotogenic models. In one version of the scotogenic model, neutrinos are Majorana. Hence, this model is called MSM. Whereas, in the other version of the model, which is called DSM, neutrinos are Dirac. In both the MSM and DSM, we have obtained the analytical expressions for the branching ratios of all the LFV decays that are tabulated in Tab. 1, in addition to finding the conversion rate of $\mu\text{Au} \rightarrow e\text{Au}$.

After scanning over the parameter space of the MSM and DSM, we have first studied constraints to be imposed by the observables $\text{Br}(\mu \rightarrow e\gamma)$, $\text{Br}(\mu \rightarrow 3e)$ and $\text{CR}(\mu \rightarrow e, \text{Au})$. While doing this analysis, we have emphasized the role played by the perturbativity bound on the Yukawa couplings. We have shown that, by satisfying the experimental limit on $\text{Br}(\mu \rightarrow e\gamma)$ and perturbativity bound on Yukawa couplings, there can exist a parameter region in both the MSM and DSM, where the experimental limit on $\text{Br}(\mu \rightarrow 3e)$ cannot be satisfied. This implies that $\text{Br}(\mu \rightarrow e\gamma)$ and $\text{Br}(\mu \rightarrow 3e)$ can give constraints of their own

on the model parameters of the MSM and DSM. We have also shown that the constraints due to $\text{Br}(\mu \rightarrow 3e)$ are stringent in the MSM in comparison to that in the DSM. This reflects to the fact that, between these two models, additional box contribution exist in the MSM. On the other hand, we have not found a region in both the MSM and DSM, where $\text{CR}(\mu \rightarrow e, \text{Au})$ exceed over the experimental limit on this observable, after satisfying the experimental limit on $\text{Br}(\mu \rightarrow e\gamma)$.

Next, we have studied LFV tau decays in both the MSM and DSM, after satisfying the experimental limits on $\text{Br}(\mu \rightarrow e\gamma)$, $\text{Br}(\mu \rightarrow 3e)$, $\text{CR}(\mu \rightarrow e, \text{Au})$ and perturbativity bound on the Yukawa couplings. We have found that the decay $\tau \rightarrow 3\mu$ can have a branching ratio which can reach to around $10^{-10}(10^{-11})$ in the MSM(DSM). This branching ratio can be probed in the future proposed experiments. We have found that, in both the MSM and DSM, the maximal reaches of the branching ratios of the LFV tau decays in the case of IO cannot exceed over that of the corresponding decays in the case of NO. We have also compared the branching ratios of the LFV tau decays between the MSM and DSM. In this comparison, we have found that the 2-body decays $\tau \rightarrow e\gamma$ and $\tau \rightarrow \mu\gamma$ can have same maximal values of the branching ratios in both the MSM and DSM. On the other hand, for the 3-body LFV tau decays, the maximal values of the branching ratios in the DSM are suppressed in comparison to that of the corresponding branching ratios in the MSM. This is vindicated by the fact that there exist additional contribution to the 3-body LFV tau decays in the MSM in comparison to that in the DSM.

References

- [1] T. Kajita, *Nobel Lecture: Discovery of atmospheric neutrino oscillations*, *Rev. Mod. Phys.* **88** (2016) 030501.
- [2] A.B. McDonald, *Nobel Lecture: The Sudbury Neutrino Observatory: Observation of flavor change for solar neutrinos*, *Rev. Mod. Phys.* **88** (2016) 030502.
- [3] PLANCK collaboration, *Planck 2018 results. VI. Cosmological parameters*, *Astron. Astrophys.* **641** (2020) A6 [[1807.06209](#)].
- [4] C. Quigg, *Beyond the standard model in many directions*, in *2nd CERN-CLAF School of High Energy Physics*, pp. 57–118, 4, 2004 [[hep-ph/0404228](#)].
- [5] J. Ellis, *Physics Beyond the Standard Model*, *Nucl. Phys. A* **827** (2009) 187C [[0902.0357](#)].

- [6] S.F. King, *Neutrino mass models*, *Rept. Prog. Phys.* **67** (2004) 107 [[hep-ph/0310204](#)].
- [7] G. Altarelli, *Models of neutrino masses and mixings*, in *61st Scottish Universities Summer School in Physics: Neutrinos in Particle Physics, Astrophysics and Cosmology (SUSSP61)*, pp. 91–115, 11, 2006 [[hep-ph/0611117](#)].
- [8] P. Minkowski, $\mu \rightarrow e\gamma$ at a Rate of One Out of 10^9 Muon Decays?, *Phys. Lett. B* **67** (1977) 421.
- [9] M. Gell-Mann, P. Ramond and R. Slansky, *Complex Spinors and Unified Theories*, *Conf. Proc. C* **790927** (1979) 315 [[1306.4669](#)].
- [10] R.N. Mohapatra and G. Senjanovic, *Neutrino Mass and Spontaneous Parity Nonconservation*, *Phys. Rev. Lett.* **44** (1980) 912.
- [11] J. Schechter and J.W.F. Valle, *Neutrino Masses in $SU(2) \times U(1)$ Theories*, *Phys. Rev. D* **22** (1980) 2227.
- [12] M. Magg and C. Wetterich, *Neutrino Mass Problem and Gauge Hierarchy*, *Phys. Lett. B* **94** (1980) 61.
- [13] R.N. Mohapatra and G. Senjanovic, *Neutrino Masses and Mixings in Gauge Models with Spontaneous Parity Violation*, *Phys. Rev. D* **23** (1981) 165.
- [14] G. Lazarides, Q. Shafi and C. Wetterich, *Proton Lifetime and Fermion Masses in an $SO(10)$ Model*, *Nucl. Phys. B* **181** (1981) 287.
- [15] R. Foot, H. Lew, X.G. He and G.C. Joshi, *Seesaw Neutrino Masses Induced by a Triplet of Leptons*, *Z. Phys. C* **44** (1989) 441.
- [16] R.N. Mohapatra, *A Model for Dirac Neutrino Masses and Mixings*, *Phys. Lett. B* **198** (1987) 69.
- [17] D. Chang and R.N. Mohapatra, *Small and Calculable Dirac Neutrino Mass*, *Phys. Rev. Lett.* **58** (1987) 1600.
- [18] R.N. Mohapatra, *Left-right Symmetry and Finite One Loop Dirac Neutrino Mass*, *Phys. Lett. B* **201** (1988) 517.

- [19] B.S. Balakrishna and R.N. Mohapatra, *Radiative Fermion Masses From New Physics at TeV Scale*, *Phys. Lett. B* **216** (1989) 349.
- [20] E. Ma, *Radiative Quark and Lepton Masses in a Left-right Gauge Model*, *Phys. Rev. Lett.* **63** (1989) 1042.
- [21] K.S. Babu and X.G. He, *DIRAC NEUTRINO MASSES AS TWO LOOP RADIATIVE CORRECTIONS*, *Mod. Phys. Lett. A* **4** (1989) 61.
- [22] G.C. Branco and C.Q. Geng, *Naturally Small Dirac Neutrino Masses in Superstring Theories*, *Phys. Rev. Lett.* **58** (1987) 969.
- [23] K.S. Babu and E. Ma, *Radiative Mechanisms for Generating Quark and Lepton Masses: Some Recent Developments*, *Mod. Phys. Lett. A* **4** (1989) 1975.
- [24] S. Nasri and S. Moussa, *Model for small neutrino masses at the TeV scale*, *Mod. Phys. Lett. A* **17** (2002) 771 [[hep-ph/0106107](#)].
- [25] E. Ma, *Verifiable radiative seesaw mechanism of neutrino mass and dark matter*, *Phys. Rev. D* **73** (2006) 077301 [[hep-ph/0601225](#)].
- [26] E. Ma, *Supersymmetric Model of Radiative Seesaw Majorana Neutrino Masses*, *Annales Fond. Broglie* **31** (2006) 285 [[hep-ph/0607142](#)].
- [27] E. Ma and U. Sarkar, *Revelations of the $E(6)/U(1)(N)$ Model: Two-Loop Neutrino Mass and Dark Matter*, *Phys. Lett. B* **653** (2007) 288 [[0705.0074](#)].
- [28] E. Ma, *$Z(3)$ Dark Matter and Two-Loop Neutrino Mass*, *Phys. Lett. B* **662** (2008) 49 [[0708.3371](#)].
- [29] E. Ma, *$SU(5)$ completion of the dark scalar doublet model of radiative neutrino mass*, *Phys. Lett. B* **659** (2008) 885 [[0710.2325](#)].
- [30] E. Ma, *Supersymmetric $U(1)$ Gauge Realization of the Dark Scalar Doublet Model of Radiative Neutrino Mass*, *Mod. Phys. Lett. A* **23** (2008) 721 [[0801.2545](#)].
- [31] P.-H. Gu and U. Sarkar, *Radiative seesaw in left-right symmetric model*, *Phys. Rev. D* **78** (2008) 073012 [[0807.0270](#)].
- [32] E. Ma and D. Suematsu, *Fermion Triplet Dark Matter and Radiative Neutrino Mass*, *Mod. Phys. Lett. A* **24** (2009) 583 [[0809.0942](#)].

- [33] A. Abada, N. Bernal, A.E. Cárcamo Hernández, S. Kovalenko, T.B. de Melo and T. Toma, *Phenomenology of a scotogenic neutrino mass model at 3-loops*, in *18th International Conference on Topics in Astroparticle and Underground Physics*, 11, 2023 [[2311.14716](#)].
- [34] A. Ahriche, M.L. Bellilet, M.O. Khojali, M. Kumar and A.-T. Mulaudzi, *The scale invariant scotogenic model: CDF-II W-boson mass and the 95 GeV excesses*, [2311.08297](#).
- [35] D. Borah, S. Mahapatra, P.K. Paul and N. Sahu, *Scotogenic $U(1)_{L_\mu-L_\tau}$ origin of $(g-2)_\mu$, W-mass anomaly and 95 GeV excess*, [2310.11953](#).
- [36] Avnish, *Maximum Yukawa Couplings for WIMP Majorana Dark Matter in Scotogenic Model*, *Phys. Part. Nucl. Lett.* **20** (2023) 1146.
- [37] L. Singh, D. Mahanta and S. Verma, *Low Scale Leptogenesis in Singlet-Triplet Scotogenic Model*, [2309.12755](#).
- [38] T. Kitabayashi, *Constraining scotogenic dark matter and primordial black holes using gravitational waves*, [2309.01883](#).
- [39] A. Karan, S. Sadhukhan and J.W.F. Valle, *Phenomenological profile of scotogenic fermionic dark matter*, [2308.09135](#).
- [40] J. Herms, S. Jana, V.P. K. and S. Saad, *Light neutrinophilic dark matter from a scotogenic model*, *Phys. Lett. B* **845** (2023) 138167 [[2307.15760](#)].
- [41] M.S. Ismael, G. Faisel and M. Alanssari, *The Impact of Dark Matter on the Related Sector of the Scotogenic Model and Its Implications*, *LHEP* **2023** (2023) 374.
- [42] P. Escribano, V.M. Lozano and A. Vicente, *A Scotogenic explanation for the 95 GeV excesses*, [2306.03735](#).
- [43] R.S. Hundi, *Lepton flavor violating Z and Higgs decays in the scotogenic model*, *Eur. Phys. J. C* **82** (2022) 505 [[2201.03779](#)].
- [44] R.S. Hundi, *$\mu \rightarrow e\gamma$ in a supersymmetric radiative neutrino mass model*, *Phys. Rev. D* **93** (2016) 015008 [[1510.02253](#)].
- [45] Y. Farzan and E. Ma, *Dirac neutrino mass generation from dark matter*, *Phys. Rev. D* **86** (2012) 033007 [[1204.4890](#)].

- [46] E. Ma and O. Popov, *Pathways to Naturally Small Dirac Neutrino Masses*, *Phys. Lett. B* **764** (2017) 142 [[1609.02538](#)].
- [47] W. Wang, R. Wang, Z.-L. Han and J.-Z. Han, *The $B - L$ Scotogenic Models for Dirac Neutrino Masses*, *Eur. Phys. J. C* **77** (2017) 889 [[1705.00414](#)].
- [48] C.-Y. Yao and G.-J. Ding, *Systematic Study of One-Loop Dirac Neutrino Masses and Viable Dark Matter Candidates*, *Phys. Rev. D* **96** (2017) 095004 [[1707.09786](#)].
- [49] J. Calle, D. Restrepo, C.E. Yaguna and O. Zapata, *Minimal radiative Dirac neutrino mass models*, *Phys. Rev. D* **99** (2019) 075008 [[1812.05523](#)].
- [50] E. Ma, *Scotogenic $U(1)_\chi$ Dirac neutrinos*, *Phys. Lett. B* **793** (2019) 411 [[1901.09091](#)].
- [51] E. Ma, *Scotogenic cobimaximal Dirac neutrino mixing from $\Delta(27)$ and $U(1)_\chi$* , *Eur. Phys. J. C* **79** (2019) 903 [[1905.01535](#)].
- [52] E. Ma, *Two-loop Z_4 Dirac neutrino masses and mixing, with self-interacting dark matter*, *Nucl. Phys. B* **946** (2019) 114725 [[1907.04665](#)].
- [53] S. Centelles Chuliá, R. Cepedello, E. Peinado and R. Srivastava, *Systematic classification of two loop $d = 4$ Dirac neutrino mass models and the Diracness-dark matter stability connection*, *JHEP* **10** (2019) 093 [[1907.08630](#)].
- [54] S. Jana, P.K. Vishnu and S. Saad, *Minimal realizations of Dirac neutrino mass from generic one-loop and two-loop topologies at $d = 5$* , *JCAP* **04** (2020) 018 [[1910.09537](#)].
- [55] J. Leite, A. Morales, J.W.F. Valle and C.A. Vaquera-Araujo, *Scotogenic dark matter and Dirac neutrinos from unbroken gauged $B - L$ symmetry*, *Phys. Lett. B* **807** (2020) 135537 [[2003.02950](#)].
- [56] S.-Y. Guo and Z.-L. Han, *Observable Signatures of Scotogenic Dirac Model*, *JHEP* **12** (2020) 062 [[2005.08287](#)].
- [57] N. Bernal, J. Calle and D. Restrepo, *Anomaly-free Abelian gauge symmetries with Dirac scotogenic models*, *Phys. Rev. D* **103** (2021) 095032 [[2102.06211](#)].

- [58] B. De, D. Das, M. Mitra and N. Sahoo, *Magnetic moments of leptons, charged lepton flavor violations and dark matter phenomenology of a minimal radiative Dirac neutrino mass model*, *JHEP* **08** (2022) 202 [[2106.00979](#)].
- [59] S. Mishra, N. Narendra, P.K. Panda and N. Sahoo, *Scalar dark matter and radiative Dirac neutrino mass in an extended $U(1)_{B-L}$ model*, *Nucl. Phys. B* **981** (2022) 115855 [[2112.12569](#)].
- [60] T.A. Chowdhury, M. Ehsanuzzaman and S. Saad, *Dark Matter and $(g - 2)_{\mu,e}$ in radiative Dirac neutrino mass models*, *JCAP* **08** (2022) 076 [[2203.14983](#)].
- [61] S.-P. Li, X.-Q. Li, X.-S. Yan and Y.-D. Yang, *Scotogenic Dirac neutrino mass models embedded with leptiquarks: one pathway to address the flavor anomalies and the neutrino masses together*, *Eur. Phys. J. C* **82** (2022) 1078 [[2204.09201](#)].
- [62] N. Hazarika and K. Bora, *A new viable mass region of dark matter and dirac neutrino mass generation in a scotogenic extension of SM*, *Int. J. Mod. Phys. A* **38** (2023) 2350051 [[2205.06003](#)].
- [63] D. Borah, P. Das and D. Nanda, *Observable ΔN_{eff} in Dirac Scotogenic Model*, [2211.13168](#).
- [64] R.S. Hundi, *Study on the global minimum and $H \rightarrow \gamma\gamma$ in the Dirac scotogenic model*, *Phys. Rev. D* **108** (2023) 015006 [[2303.04655](#)].
- [65] P.F. de Salas, D.V. Forero, S. Gariazzo, P. Martínez-Miravé, O. Mena, C.A. Ternes et al., *2020 global reassessment of the neutrino oscillation picture*, *JHEP* **02** (2021) 071 [[2006.11237](#)].
- [66] MEG II collaboration, *A search for $\mu^+ \rightarrow e^+ \gamma$ with the first dataset of the MEG II experiment*, *Eur. Phys. J. C* **84** (2024) 216 [[2310.12614](#)].
- [67] BABAR collaboration, *Searches for Lepton Flavor Violation in the Decays $\tau_{+-} \rightarrow e_{+-} \gamma$ and $\tau_{+-} \rightarrow \mu_{+-} \gamma$* , *Phys. Rev. Lett.* **104** (2010) 021802 [[0908.2381](#)].
- [68] BELLE collaboration, *Search for lepton-flavor-violating tau-lepton decays to $\ell\gamma$ at Belle*, *JHEP* **10** (2021) 19 [[2103.12994](#)].
- [69] SINDRUM collaboration, *Search for the Decay $\mu^+ \rightarrow e^+ e^+ e^-$* , *Nucl. Phys. B* **299** (1988) 1.

- [70] K. Hayasaka et al., *Search for Lepton Flavor Violating Tau Decays into Three Leptons with 719 Million Produced Tau+Tau- Pairs*, *Phys. Lett. B* **687** (2010) 139 [[1001.3221](#)].
- [71] SINDRUM II collaboration, *A Search for muon to electron conversion in muonic gold*, *Eur. Phys. J. C* **47** (2006) 337.
- [72] SINDRUM II collaboration, *Test of lepton flavor conservation in $\mu \rightarrow e$ conversion on titanium*, *Phys. Lett. B* **317** (1993) 631.
- [73] T. Toma and A. Vicente, *Lepton Flavor Violation in the Scotogenic Model*, *JHEP* **01** (2014) 160 [[1312.2840](#)].
- [74] J.A. Casas and A. Ibarra, *Oscillating neutrinos and $\mu \rightarrow e, \gamma$* , *Nucl. Phys. B* **618** (2001) 171 [[hep-ph/0103065](#)].
- [75] PARTICLE DATA GROUP collaboration, *Review of Particle Physics*, *PTEP* **2022** (2022) 083C01.
- [76] W. Grimus and L. Lavoura, *Soft lepton flavor violation in a multi Higgs doublet seesaw model*, *Phys. Rev. D* **66** (2002) 014016 [[hep-ph/0204070](#)].
- [77] J. Kubo, E. Ma and D. Suematsu, *Cold Dark Matter, Radiative Neutrino Mass, $\mu \rightarrow e\gamma$, and Neutrinoless Double Beta Decay*, *Phys. Lett. B* **642** (2006) 18 [[hep-ph/0604114](#)].
- [78] Y. Kuno and Y. Okada, *Muon decay and physics beyond the standard model*, *Rev. Mod. Phys.* **73** (2001) 151 [[hep-ph/9909265](#)].
- [79] H.C. Chiang, E. Oset, T.S. Kosmas, A. Faessler and J.D. Vergados, *Coherent and incoherent (μ -, e -) conversion in nuclei*, *Nucl. Phys. A* **559** (1993) 526.
- [80] T.S. Kosmas, S. Kovalenko and I. Schmidt, *Nuclear muon- e - conversion in strange quark sea*, *Phys. Lett. B* **511** (2001) 203 [[hep-ph/0102101](#)].
- [81] R. Kitano, M. Koike and Y. Okada, *Detailed calculation of lepton flavor violating muon electron conversion rate for various nuclei*, *Phys. Rev. D* **66** (2002) 096002 [[hep-ph/0203110](#)].

- [82] E. Arganda, M.J. Herrero and A.M. Teixeira, *mu-e conversion in nuclei within the CMSSM seesaw: Universality versus non-universality*, *JHEP* **10** (2007) 104 [[0707.2955](#)].
- [83] BELLE-II collaboration, *The Belle II Physics Book*, *PTEP* **2019** (2019) 123C01 [[1808.10567](#)].
- [84] FCC collaboration, *FCC Physics Opportunities: Future Circular Collider Conceptual Design Report Volume 1*, *Eur. Phys. J. C* **79** (2019) 474.